Brigham Young University
BYU ScholarsArchive

All Theses and Dissertations

2007-10-12

Integrated Piezoresistive Sensing for Feedback Control of Compliant MEMS

Robert K. Messenger
Brigham Young University - Provo

Follow this and additional works at: https://scholarsarchive.byu.edu/etd

Part of the Mechanical Engineering Commons

BYU ScholarsArchive Citation

Messenger, Robert K., "Integrated Piezoresistive Sensing for Feedback Control of Compliant MEMS" (2007). *All Theses and Dissertations*. 1202.
https://scholarsarchive.byu.edu/etd/1202

This Dissertation is brought to you for free and open access by BYU ScholarsArchive. It has been accepted for inclusion in All Theses and Dissertations by an authorized administrator of BYU ScholarsArchive. For more information, please contact scholarsarchive@byu.edu, ellen_amatangelo@byu.edu.

INTEGRATED PIEZORESISTIVE SENSING FOR FEEDBACK CONTROL OF COMPLIANT MEMS

by

Robert K. Messenger

A dissertation submitted to the faculty of

Brigham Young University

in partial fulfillment of the requirements for the degree of

Doctor of Philosophy

Department of Mechanical Engineering

Brigham Young University

December 2007

Copyright © 2007 Robert K. Messenger

All Rights Reserved

BRIGHAM YOUNG UNIVERSITY

GRADUATE COMMITTEE APPROVAL

of a dissertation submitted by

Robert K. Messenger

This dissertation has been read by each member of the following graduate committee and by majority vote has been found to be satisfactory.

Date	Timothy W. McLain, Chair
Date	Larry L. Howell
Date	Brian D. Jensen
Date	Craig C. Smith
Date	Aaron R. Hawkins

BRIGHAM YOUNG UNIVERSITY

As chair of the candidate's graduate committee, I have read the dissertation of Robert K. Messenger in its final form and have found that (1) its format, citations, and bibliographical style are consistent and acceptable and fulfill university and department style requirements; (2) its illustrative materials including figures, tables, and charts are in place; and (3) the final manuscript is satisfactory to the graduate committee and is ready for submission to the university library.

Date

Timothy W. McLain
Chair, Graduate Committee

Accepted for the Department

Matthew R. Jones
Graduate Coordinator

Accepted for the College

Alan R. Parkinson
Dean, Ira A. Fulton College of
Engineering and Technology

ABSTRACT

INTEGRATED PIEZORESISTIVE SENSING FOR FEEDBACK CONTROL OF COMPLIANT MEMS

Robert K. Messenger

Department of Mechanical Engineering

Doctor of Philosophy

Feedback control of MEMS devices has the potential to significantly improve device performance and reliability. One of the main obstacles to its broader use is the small number of on-chip sensing options available to MEMS designers. A method of using integrated piezoresistive sensing is proposed and demonstrated as another option. Integrated piezoresistive sensing utilizes the inherent piezoresistive property of polycrystalline silicon from which many MEMS devices are fabricated. As compliant MEMS structures flex to perform their functions, their resistance changes. That resistance change can be used to transduce the structures' deflection into an electrical signal. This dissertation addresses three topics associated with integrated piezoresistive sensing: developing an empirical model describing the piezoresistive response of polycrystalline-silicon flexures, designing compliant MEMS with integrated piezoresistive sensing using the model, and implementing feedback control using integrated piezoresistive sensing.

Integrated piezoresistive sensing is an effective way to produce small, reliable, accurate, and economical on-chip sensors to monitor compliant MEMS devices. A piezoresistive flexure model is presented that accurately models the piezoresistive response of long, thin flexures even under complex loading conditions. The model facilitates the design of compliant piezoresistive MEMS devices, which output an electrical signal that directly relates to the device's motion.

The piezoresistive flexure model is used to design a self-sensing long displacement MEMS device. Motion is achieved through contact-aided compliant rolling elements that connect the output shaft to kinematic ground. Self-sensing is achieved though integrated piezoresistive sensing. An example device is tested that demonstrates 700 micrometers of displacement with a sensing resolution of 2 micrometers.

The piezoresistive microdisplacement transducer (PMT) is a structure that uses integrated piezoresistive sensing to monitor the output displacement of a thermomechanical inplane microacutator (TIM). Using the PMT as a feedback sensor for closed-loop control of the TIM reduced the system's response time from 500 μs to 190 μs, while maintaining a positioning accuracy of $\pm$29 nm. Feedback control of the TIM also increased its robustness and reliability by allowing the system to maintain its performance after it had been significantly damaged.

ACKNOWLEDGMENTS

This work was supported by a host of people and institutions. Without them this research would not have been possible. Brigham Young University provided equipment, facilities, and many educational opportunities. The mechanical engineering faculty did an excellent job of teaching me the required skills. The faculty that served on my committee mentored me and guided my efforts. I especially thank Dr. McLain and Dr. Howell for their efforts on my behalf over the years.

This study was supported financially by the National Science Foundation under grant number CMS-0428532. Additionally Sandia National Laboratories and Block MEMS, LLC provided support with testing facilities and fabrication.

Many of the interactions I had with my fellow students were invaluable in keeping this work moving. The Compliant Mechanisms Research Lab has been a great environment that fosters creative and productive work. Some specific contributions include Quentin Aten assisting me in circuit assembly and electrical noise isolation, Gerrit Larsen had the insight of approximating piezoresistive bending structures as two parallel resistors, and Scott Lyon came up with the idea of using floating power supplies to isolate sensing signals from actuation signals.

As always, my family have been my greatest supporters.

Table of Contents

Acknowledgements **xiii**

List of Figures **xx**

1 Introduction **1**

1.1 Background 1

1.1.1 Surface micromachining 2

1.1.2 Compliant mechanisms 2

1.1.3 Piezoresistivity 3

1.2 Motivation 4

1.3 Approach 5

1.4 Contributions 6

1.5 Document Organization 6

2 Piezoresitive Response of Polycrystalline-silicon Flexures **9**

2.1 Introduction 9

2.1.1 Integrated piezoresistive sensing 11

2.2 Traditional Piezoresistive Sensing 12

2.3 Integrated Piezoresistive Sensing — Axial 12

2.3.1 Piezoresistive Bending 15

2.4 Integrated Piezoresistive Sensing — Bending 18

2.5 Integrated Piezoresistive Sensing — Combined 21

2.6 Conclusion 23

3 A Self-Sensing Long-Displacement MEMS Device 25

3.1 Introduction 25

3.1.1 Piezoresistive contact-aided linear mechanism 26

3.2 Mechanical Design 28

3.3 Piezoresistive Response 32

3.3.1 Experimental results 34

3.4 Conclusion 36

4 Feedback Control of a MEMS Thermal Acutator 37

4.1 Introduction 37

4.1.1 Piezoresistivity of polysilicon 38

4.1.2 Thermomechanical inplane microactuator 39

4.2 Piezoresistive Microdisplacement Transducer 40

4.2.1 Piezoresistive response of the PMT 43

4.2.2 Sensor characterization 45

4.2.3 Dynamic performance 47

4.2.4 Parasitic capacitance 50

4.3 Control Design 52

4.3.1 Proportional control 53

4.3.2 Integral-lead control 54

4.3.3 Steady-state control in a vacuum 55

4.3.4 Position control results 56

4.3.5 Disturbance rejection 57

4.4 Conclusion 58

5 Conclusion **61**

5.1 Summary of Contributions 61

5.2 Suggested Future Work 62

Bibliography **63**

List of Figures

1.1 Images illustrating the surface micromachining process. 3

2.1 Traditional MEMS piezoresistive sensing. 10

2.2 Integrated piezoresistive sensing with axial loading. 13

2.3 Axial loading test structure. 13

2.4 Piezoresistive response of axially loaded flexures. 15

2.5 Integrated piezoresistive sensing of a flexure in bending. 16

2.6 Two parallel resistors analogy for bending. 17

2.7 Bending loads test structure. 19

2.8 Piezoresistive response of flexures in bending. 20

2.9 Combined loading test structure. 21

2.10 FEA simulation of combined loading structure. 22

2.11 Combined-load test structure's piezoresistive response. 23

3.1 Rolling linear mechanism schematic. 27

3.2 No-slip condition via compliant flexures. 27

3.3 Self sensing via piezoresistive flexures. 27

3.4 Image of piezoresistive contact-aided linear mechanism. 28

3.5 Comparison of cantilever and contact-aided flexures. 30

3.6 SEM of a roller as fabricated. 31

3.7 SEM of a displaced roller. 32

3.8 SEM of a displaced flexure. 32

3.9 Stress profile of a contact-aided flexure. 33

3.10 Piezoresistive response of long-displacement device. 35

4.1 Thermomechanical Inplane Microactuator 38

4.2 Physical schematic of the TIM/PMT setup. 41

4.3 FEA of PMT stress distribution. 41

4.4 Electrical schematic of the PMT. 42

4.5 SEM of the TIM/PMT setup. 42

4.6 Predicted PMT output versus displacement. 44

4.7 PMT output versus displacement. 45

4.8 PMT output versus displacement in a vacuum. 48

4.9 Open-loop response of TIM/PMT system. 49

4.10 Open-loop freqency response of the TIM/PMT system. 50

4.11 Parasitic capacitance schematic 51

4.12 Lumped model dynamics analysis 52

4.13 Feedback control (closed loop) block diagram. 53

4.14 Proportional-control step response. 53

4.15 Schematic of integral-lead control implementation. 55

4.16 Integral-lead control tracking performance. 55

4.17 Open-loop nanopositioning data and regression. 57

4.18 Closed-loop nanopositioning data and regression. 57

4.19 Image of damaged TIM. 58

4.20 Closed-loop disturbance rejection performance. 58

Chapter 1

Introduction

Microelectromechanical Systems (MEMS) have the potential to benefit a number of important technology fields including communications, biomedicine, national defense, public safety, transportation, video displays, and many others. Exciting and innovative MEMS technologies have been developed by academic and other research groups. However, there have been few MEMS successes in a production environment. A key obstacle to successful development of MEMS products is the difficulty in producing complex micro-scale devices that perform adequately and reliably. Complications such as planar fabrication, impractical assembly, spatial uncertainty, dominating surface forces, and poor system state monitoring arise when working in small-scale environments. While the use of compliant mechanisms and thermal actuation has been used to mitigate some of the complications, this study will expand their theory of use to include integrated piezoresistive sensing for feedback control of the system. Effective and economic feedback control is a crucial capability for MEMS technology success.

1.1 Background

The term Microelectromechanical Systems and its associated acronym MEMS were probably first coined in 1989 by a group of about 80 researchers gathered at the Micro-Tele-Operated Robotics Workshop in Salt Lake City [1]. MEMS described the emerging technology of using semiconductor fabrication techniques to create machines. MEMS are micro-scale devices—such as sensors, mechanisms, and actuators—that operate not only in the electrical domain, but in other energy domains as well. The term MEMS has expanded to include just about any device, technology, or

fabrication technique that can be described by micrometer-size (10^{-6} m or μm) characteristic dimensions. For example, devices fabricated using LIGA technology, its related micromolding fabrication techniques, and even micro wire-EDM are considered MEMS in addition to traditional bulk micromachined and surface micromachined devices. Automotive airbag acceleromenters, inertial navigation accelerometers, projection displays, DC-shunt microswitches, pressure sensors, chemical and biological sensors, optical switches, DNA sequencing, and ink-jet print nozzles are some examples of current MEMS applications [1, 2, 3, 4].

1.1.1 Surface micromachining

This study will consider polycrystalline-silicon surface-micromachined MEMS devices. Surface micromachining of polycrystalline-silicon structures is accomplished as follows. Alternating layers of silicon oxide and polycrystalline-silicon are deposited on a silicon substrate using chemical vapor deposition (CVD). After each layer is deposited it is lithographically patterned and then selectively etched away to create the desired geometry. The device is then "released" by dissolving the silicon oxide layers with hydrofluoric acid. Once the sacrificial oxide layers are removed, the remaining polycrystalline-silicon structure is free to move. Figure 1.1(a) illustrates the process for a single polycrystalline-silicon layer. Figure 1.1(b) is a Scanning Electron Micrograph (SEM) of a pin joint fabricated from four polycrystalline-silicon layers using Sandia National Laboratories' SUMMiT V process [5]. The pin joint has been sectioned with a focused ion beam to reveal the layers. Figure 1.1(c) is a MEMS device fabricated from two polycrystalline-silicon layers using MEMSCAP's MUMPS process [6].

1.1.2 Compliant mechanisms

Compliant mechanisms have proven to be an enabling technology for micro-scale devices and particularly for MEMS with planar fabrication methods such as surface micromachining. Compliant mechanisms are devices that use deformation of part of the device to perform the desired function [7]. Compliant mechanisms

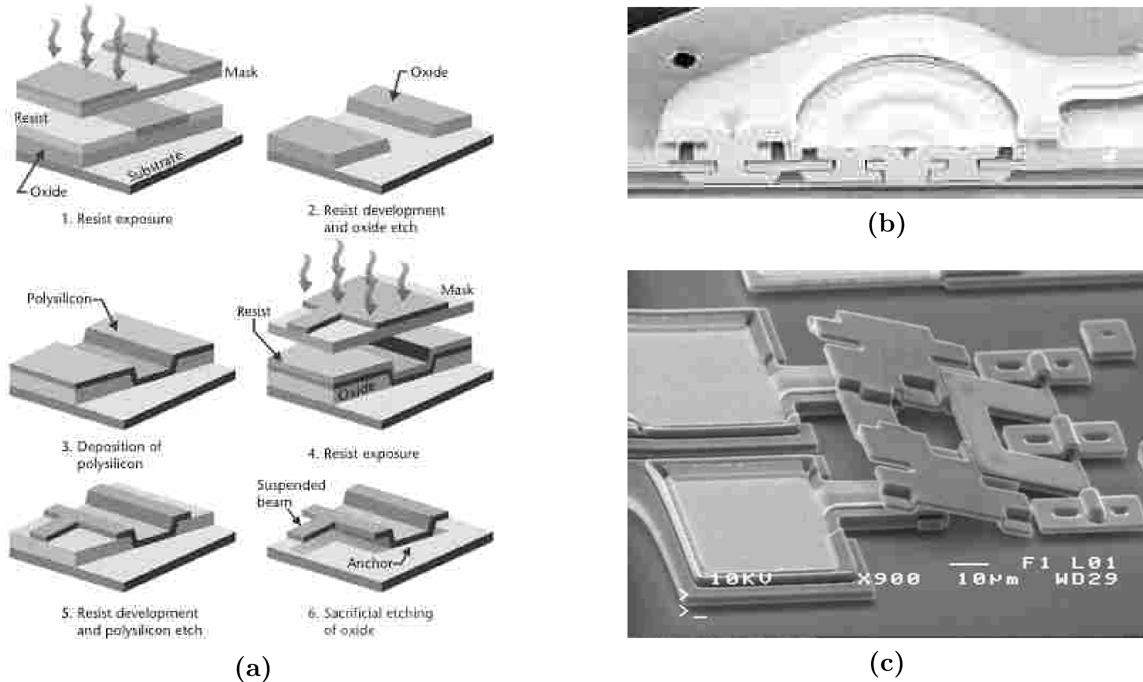

Figure 1.1: Images illustrating the surface micromachining process – (a) schematic of the process steps[1], (b) pin joint that has been sectioned with a focused ion beam[2], and (c) a simple example.

have several significant advantages for MEMS devices. They can be fabricated using planar layers of materials and require no assembly, enabling fabrication of complex mechanisms using existing fabrication methods. They have no friction from rubbing parts, exhibit no wear, and do not experience backlash. As a result, they provide high-precision motion that is more repeatable and more predictable.

1.1.3 Piezoresistivity

Many MEMS devices are fabricated from polycrystalline-silicon that is heavily doped with elements such as phosphorus to improve electrical conduction. As silicon is a semiconducting material, the doping also makes it significantly piezoresistive.

A piezoresistive material exhibits a change in electrical resistance when a mechanical load is applied. Metal piezoresistivity is the result of volumetric changes in the structure, such as lengthening of the current path when a wire is in tension.

[1]Image courtesy of N. Maluf [1].
[2]Image courtesy of Sandia National Laboratories.

However, semiconductor piezoresistors experience a change in the resistivity of the material itself. The semiconductor piezoresistive effect is up to two orders of magnitude greater than metal piezoresistivity [8]. While the exact mechanism that causes semiconductor piezoresistivity is not definitively known, it is hypothesized that mechanical strain changes the crystal structure of the material, altering the band-gap energy to either inhibit or ease electron flow. Piezoresistivity is the mechanism used to enable a variety of MEMS sensors. For example, it has been used for accelerometers [9], pressure sensors [10], and on-chip microphones [11].

1.2 Motivation

Feedback control can mitigate the large performance variations inherent in MEMS devices. Effects such as surface forces causing stiction, fabrication variables producing uncertainties in device dimensions and material properties, and other environmental factors have a large influence on machines operating at the micro scale. Feedback provides improved dynamic response, precision performance, and reliability.

At the micro scale, and particularly with surface micromachined devices, implementation of feedback control faces distinct challenges imposed by size and complexity constraints. For example, due to the small size of the devices, the signal-to-noise ratio produced by feedback transducers is usually poor. The typical way to compensate for this is to fabricate the control circuitry on the same die as the MEMS. Unfortunately, this requires challenging and expensive custom fabrication processes resulting in compromises in both the MEMS and circuitry design.

Another sensing solution used in laboratory setups is off-chip sensing. Devices such as laser doppler vibrometers [12] and laser interferometers [13] have been used to provide accurate real-time measurements of microdevice operations. However, these are not desirable solutions for anything other than prototypes or expensive, low-volume products.

1.3 Approach

Previous work has demonstrated the feasibility of using the inherent piezoresistivity of MEMS polycrystalline-silicon for a feedback sensing mechanism [14, 15, 16]. Therefore, it is possible to observe the deformation of a MEMS compliant mechanism by measuring the resistance across particular portions of the mechanism. This allows for direct integration of the sensor into the device. This study develops a method for designing compliant MEMS devices with integrated piezoresistive sensing. This study also demonstrates that integrated piezoresistive sensing enables practical and effective feedback control of compliant MEMS devices.

Design of compliant MEMS with integrated piezoresistive sensing requires a model which will predict the piezoresistive response of an arbitrary compliant structure. Most compliant MEMS structures operate through the deflection of long thin flexures. By using a piezoresistive model that is limited to long thin flexures, the model can be accessible for design calculation and general enough to apply in most cases. The model presented here is empirical, and is developed from the synthesis of experimental piezoresistive response data and analytical stress formulation.

As a demonstration and validation, the piezoresistive flexure model is used to design a self-sensing long-displacement MEMS device. This is a novel and useful structure that is capable of up to 700 μm of displacement and uses integrated piezoresistive sensing for a displacement measurement resolution of 2 μm. The design study demonstrates how to design piezoresistive flexures for a compliant mechanism and predict their piezoresistive response.

A case study involving integrated piezoresistive sensing for feedback control completes the development. A Thermomechanical Inplane Microactuator (TIM), a MEMS device that amplifies motion caused by thermal expansion, is characterized and feedback controlled using integrated piezoresistive sensing. TIMs have large output forces and displacements for micro-acutators, and are often coupled with compliant mechanisms. They also have interesting dynamics due to the nonlinear nature of their thermal and mechanical responses. An effective control scheme is identified to compensate for the TIM's slow response time and steady-state error. The integrated

piezoresistive sensing is provided by a proven structure known as a Piezoresistive Microdisplacement Transducer (PMT) [15, 16]. The PMT is empirically characterized, enabling fine control of the TIM displacement.

1.4 Contributions

This dissertation makes the following contributions associated with integrated piezoresistive sensing of compliant MEMS devices.

- Validation of piezoresistive sensing's effectiveness for compliant MEMS devices via the measured piezoresistive response of a variety of MEMS devices.
- Development of an accessible predictive model, useful for design of long thin piezoresistive flexures.
- Validation of the piezoresistive model via the design and testing of a self-sensing long-displacement MEMS device.
- Identification of an effective feedback control scheme to improve the performance and reliability of the TIM.
- Implementation of feedback control, using integrated piezoresistive sensing, and verification of the predicted performance and reliability improvements.

1.5 Document Organization

The majority of this document is composed of three papers, each describing a step of the method outlined above. Each paper was written to stand alone as they are intended for peer-reviewed archival publication. However, the paper introductions have been supplemented for this dissertation to aid with transitions and keep the papers in context with the entire study.

Chapter 2 is from a paper titled, "A Model for the Piezoresistive Response of Polycrystalline-Silicon Flexures." It details the development of an empirical model that predicts the piezoresistive response of MEMS flexures under complex loading conditions.

Chapter 3 is from a paper titled, “A Self-Sensing Long-Displacement MEMS Device.” It describes the design and testing of a MEMS device that provides up to 700 μm of linear translation and uses integrated piezoresistive sensing to measure that displacement.

Chapter 4 is from a paper titled, ”Piezoresistive Feedback Control of a MEMS Thermal Actuator.” This is a case study demonstrating how feedback control can be implemented on a TIM using integrated piezoresistive sensing.

A conclusion follows these papers in Chapter 5 that ties the papers together, summarizes the major contributions, and suggests further work.

Chapter 2

Piezoresitive Response of Polycrystalline-silicon Flexures

2.1 Introduction

Integrated piezoresistive sensing involves compliant members where both mechanical and electrical phenomenon are involved. Both energy domains are critical to the functionality of the mechanisms. Therefore, it is necessary to have a model that accurately predicts the interaction between mechanical deformation and electrical resistivity. It is important for the model to be accessible because design is typically an iterative process. An accessible model can also provide the designer with helpful insights. If the model is unwieldy it can only be effectively used for validation of a design instead of exploration for a design.

Piezoresistance is a change in electrical resistance due to an applied stress. Smith showed that both p and n type silicon demonstrate a larger piezoresistive effect than that exhibited in metals [8]. Ductile metals, for example metal foil strain gauges, change resistance due to volumetric effects. Metal structures stretch and compress under axial loads changing the cross sectional area and length of the current path. For long thin current paths with a constant cross section, the resistance

$$R = \rho \frac{\ell}{a}, \tag{2.1}$$

is proportional to the length, ℓ, and inversely proportional to the cross sectional area, a.

However, volumetric effects cannot account for the magnitude of resistance change that Smith discovered. Silicon is a brittle material that deforms much less than a ductile metal under the same load, and yet it exhibits a resistance change

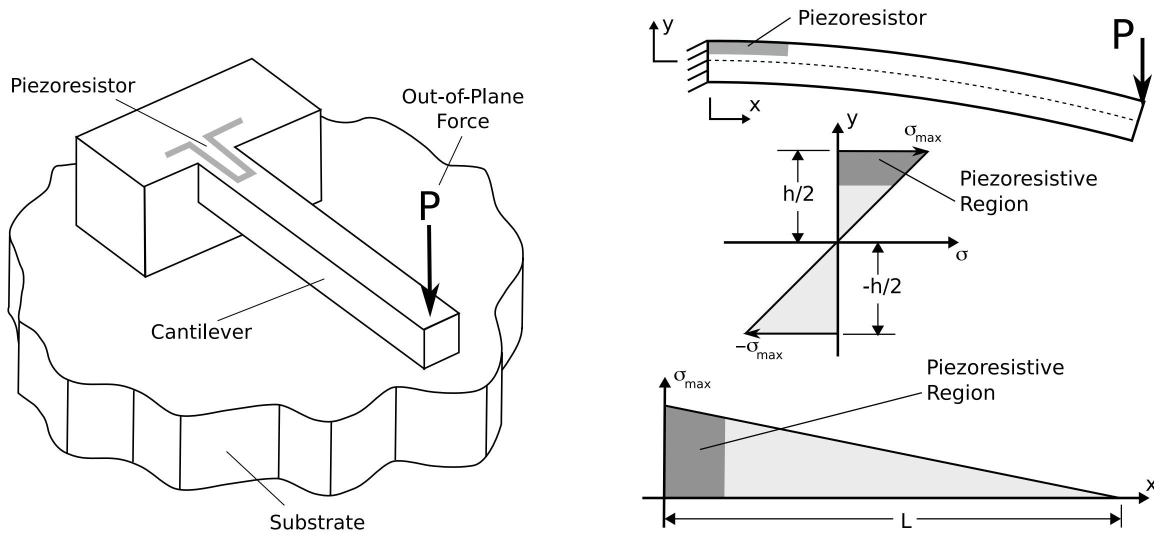

Figure 2.1: Traditional MEMS piezoresistive sensing involves fabricating a piezoresistive sensing region on top of a flexure or membrane at the location of greatest axial stress.

up to two orders of magnitude larger. Furthermore, in certain cases silicon changes resistance opposite to that explained by volumetric piezoresistance; it decreases resistance as ℓ gets larger and a gets smaller. From equation (2.1), we can conclude that the resistivity, ρ, of silicon itself changes. While the exact mechanism for silicon piezoresistivity is not known, it is hypothesized that the inter-atomic spacing of the silicon crystal structure changes when the material is stressed. This change in crystal structure increases or decreases silicon's semiconductor band-gap energy, thus facilitating or inhibiting electron movement [17, 18, 19, 20, 21].

Silicon piezoresistivity is a useful property for implementing transducers between the mechanical and electrical energy domains. Piezoresistive silicon has been used to develop many MEMS based sensors including pressure sensors [10], accelerometers [9], and microphones [11].

In this study we examine piezoresistive phenomena in surface micromachined MEMS devices where the structural layers are formed using polycrystalline silicon. Most MEMS-based piezoresistive sensors are fabricated using bulk micromachining where the devices are etched out of the monocrystalline substrate itself. Monocrystalline silicon exhibits a greater piezoresistive effect than polycrystalline silicon. How-

ever, polycrystalline silicon is significantly piezoresistive and many surface micromachined sensors have been developed with strong, well-behaved responses [10, 22, 23, 24]. Surface micromachining also provides greater flexibility in designing multilayer geometries and complex current paths.

2.1.1 Integrated piezoresistive sensing

Many successful MEMS devices rely on long, thin flexures for their functionality. These flexures experience complex, yet predictable stresses throughout their volumes as they deflect. Commercial MEMS processes typically use heavily doped structural layers to provide sufficient conductivity. As a result, the structural layers are entirely piezoresistive[1]. It is therefore possible to implement integrated piezoresistive sensing by routing a conduction path through the flexures. As the flexures' stress profiles change during their motions their resistance will also change. Integrated piezoresistive sensing transduces mechanical compliant motion into electrical signals for direct monitoring of the MEMS device. This is different than the traditional approach in that the sensor is implemented using uniformly doped polysilicon instead of patterned regions of piezoresistivity.

Some reasonable simplifying assumptions can be made in order to develop an accessible design methodology. Most compliant mechanisms are composed of long thin flexures. Long thin flexures have negligible shear stress and their neutral axes are effectively coincidental with their centroidal axes — even for initially curved flexures. As such, the modeling of compliant structures with integrated piezoresistive sensing reduces to modelling the piezoresistive response of long thin flexures to axial and bending loads. In addition to assuming negligible shear and a centrally located neutral axes, polycrystalline silicon is also assumed to be isotropic and linearly elastic for this study.

[1]For example, both the MUMPs [6] and the SUMMiT [5] processes exhibit strong piezoresistive behavior [21].

2.2 Traditional Piezoresistive Sensing

We will begin our study by examining the traditional approach for implementing piezoresistive sensing in MEMS devices. This will lay a groundwork for extending the model so it is effective for integrated piezoresistive sensing.

Extensive work applying Smith's piezoresistive model to the random crystal orientations of polycrystalline silicon has validated his model for axial loading conditions [19]. For example, a typical surface-micromachined piezoresistive device is composed of a beam or a membrane that deflects in response to some physical phenomenon. The deflection is typically out-of-plane i.e. orthogonal to the substrate. A piezoresistive region is fabricated on top of the structure in a location that experiences the most stress, and the stress is purely axial (compression or tension) because the piezoresistive region is located exclusively above the neutral axes of the beam or membrane. This is clearly illustrated in Figure 2.1 showing a cantilever beam with typical piezoresistive sensing.

In this figure the beam has height h, length L, and is loaded by force P. By locating the piezoresistor completely above the neutral axes ($y = 0$), the stress (σ) in the piezoresistive region is exclusively positive. If the load is reversed, the piezoresistive region will experience negative stress. It is also good practice to place the piezoresistor as close to the fixed end as possible because that is where the largest stresses occur.

2.3 Integrated Piezoresistive Sensing — Axial

While the standard approach to MEMS piezoresistive sensing, as illustrated in Figure 2.1, takes advantage of one highly stressed region of the beam, it ignores the stresses in the rest of the beam. Volumetrically, the majority of the beam does not contribute to the piezoresistive sensing function. The standard approach also requires a separate process step to deposit or selectively dope the piezoresistive region.

A basic example of integrated piezoresistive sensing is demonstrated by a piezoresistive beam loaded axially in tension or compression as shown in Figure 2.2. The beam in this figure experiences uniform tension or compression just like the

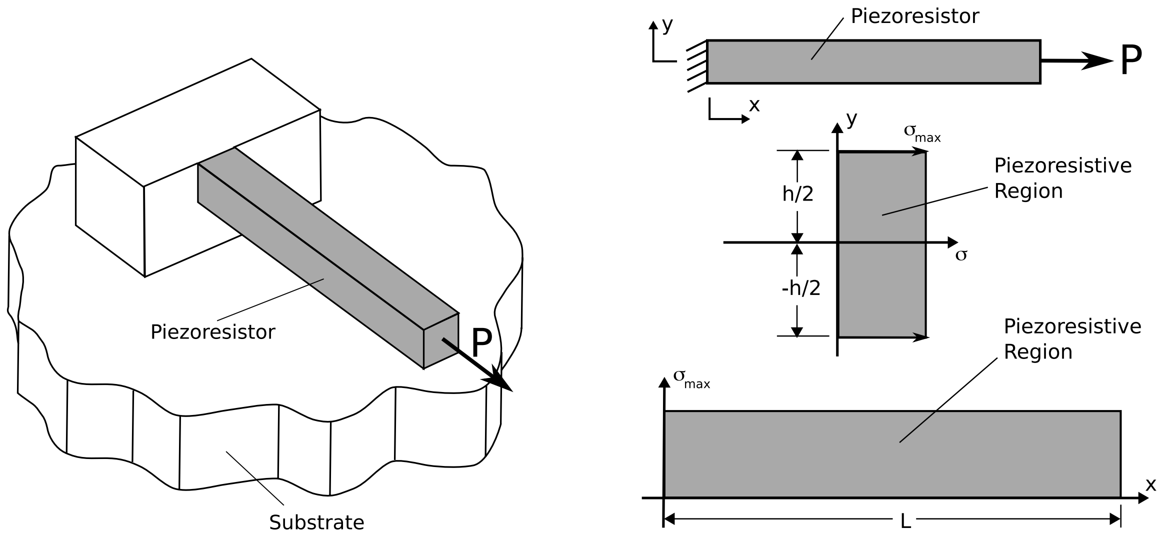

Figure 2.2: Integrated piezoresistive sensing utilizes the inherent piezoresistivity of the flexure itself, thus the entire flexure is involved in sensing. This is straightforward for flexures with purely axial loading.

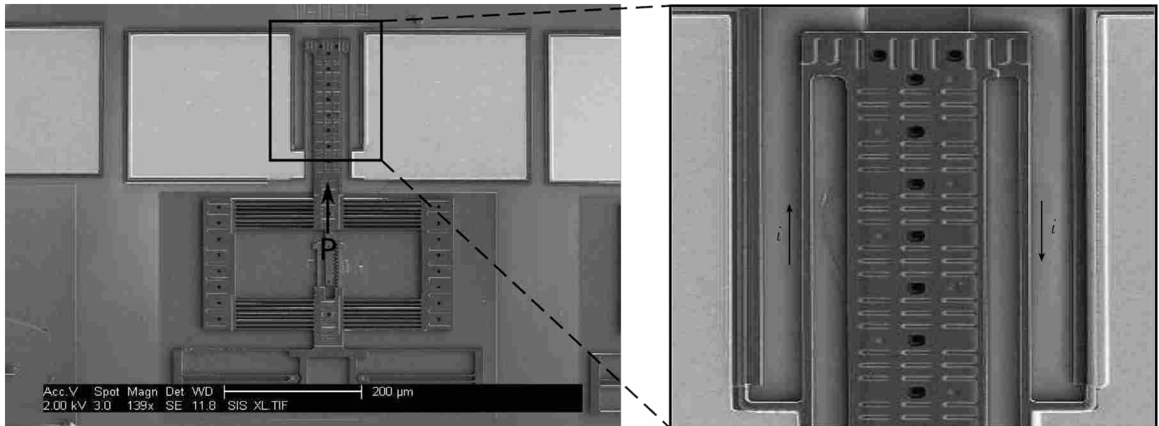

Figure 2.3: Piezoresistive coefficients for axial loading are determined experimentally using an axially loaded test structure.

piezoresistive element in Figure 2.1. But in this case the entire beam is involved in the sensing and no additional process steps were required to fabricate the sensor.

Waterfall [21] established that this implementation of integrated piezoresistive sensing behaves as expected according to Smith's model such that

$$\frac{\Delta\rho}{\rho} = \pi_A \sigma_A. \tag{2.2}$$

The fractional change in resistivity, $\Delta\rho/\rho$, is linearly related to the axial stress, σ_A, by a peizoresistive coefficient, π_A. The stress is constant and positive along the beam, and is given by

$$\sigma_A = \frac{P}{a} \tag{2.3}$$

for long, thin beams with axial-only loading.

Wheatstone bridges are typically used to turn a piezoresistive structure's change in resistivity into a voltage output. Four identical piezoresistive flexures (one for sensing and the other three for non-sensing references) form a well balanced Wheatstone bridge that produces a voltage that is a function of the fractional change in resistance of the sensing flexure

$$V_{out} = \frac{\Delta R/R}{4 + 2(\Delta R/R)} V_{in}. \tag{2.4}$$

Constructing the bridge from four identical, co-located flexures also provides for thermal compensation.

Combining equations (2.1) and (2.2), the fractional change in resistance due to an axial load is

$$\frac{\Delta R_A}{R} = \frac{\rho \pi_A \sigma_A \ell / a}{\rho \ell / a},$$

which reduces to

$$\frac{\Delta R_A}{R} = \pi_A \sigma_A. \tag{2.5}$$

The axial piezoresistive coefficient, π_A can be determined for each polycrystalline silicon layer by using a structure like the one shown in Figure 2.3. A force P is applied by deflecting a force gauge that is formed by a series of flexures. The magnitude of the force is determined by measuring the deflection of the force gauge and multiplying it by the spring constant of the force gauge [25]. This force applies uniform tensile stress to two long thin beams. Current is passed through these beams to measure their resistance at various loads.

Tensile test data was taken with beams that were fabricated from both structural layers of the MUMPs process (poly1 and poly2), and from a beam that is a

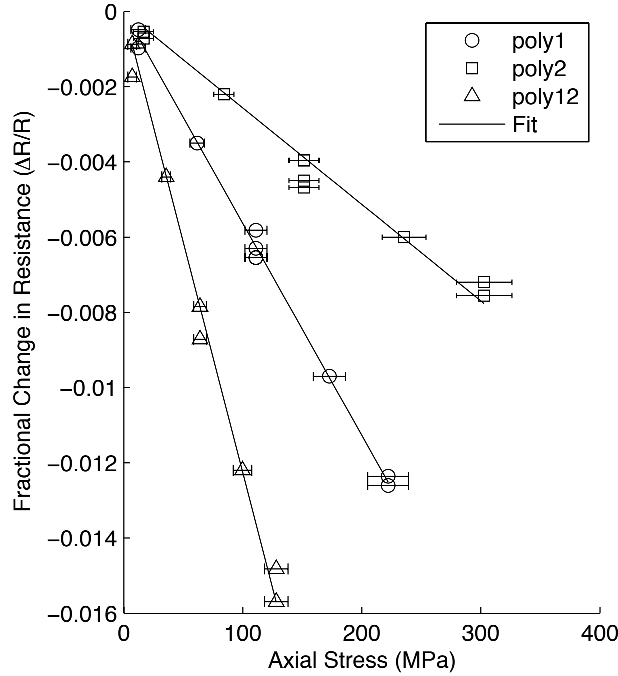

Figure 2.4: The piezoresistive response of flexures loaded axially is linear as expected. This data was taken using the devices like the one shown in Figure 2.3.

laminate of both layers (poly12). The data was taken in random order, and with enough replication to provide an estimate of the experimental uncertainty. The experimental results and linear fits are shown in Figure 2.4.

No significant curvature was found in the piezoresistive response for any of the structural layers, which matches expectations from Smith's model. While there is some variation from a linear response evident in Figure 2.4, it is close enough for a design tool. The data fits a linear response to an R^2 value of 0.97 or greater. The axial piezoresistive coefficients for poly1, poly2, and poly12 are -56.4×10^{-6}, -25.7×10^{-6}, and -122.6×10^{-6} MPa^{-1} respectively. A similar linear response has been observed for some of SUMMiT's structural layers [21].

2.3.1 Piezoresistive Bending

While axially loaded beams will adequately transduce a force or stress into an electrical signal, they only allow small deflections. MEMS flexures often undergo bending loads to achieve the large deflections required for useful compliant devices.

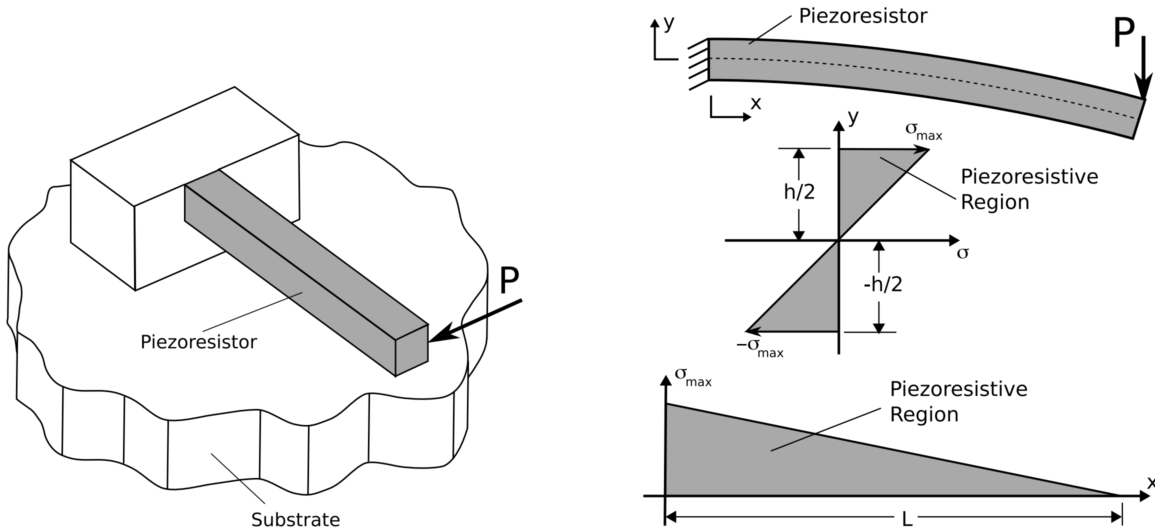

Figure 2.5: Polycrystalline-silicon flexure under bending loads also exhibit a piezoresistive response, and provide much greater deflection than axially loaded flexures.

Unfortunately, the stress and the piezoresistive effect of flexures experiencing bending loads are not as easily modeled as those of axially loaded flexures.

Most bending flexures can be reduced to a series of end-loaded cantilever beams like the one shown in Figure 2.5. In this case h is measured parallel to the plane of the substrate. Axial and shear stresses can be neglected as long as $L \gg h$. Waterfall [21] has demonstrated that bending flexures also experience piezoresistive effects in a predictable and usable manner. However, the observed piezoresistive response does not agree with what is expected from applying the axial piezoresistive model (equation (2.2)) to the bending stress distribution.

Johns [26] confirmed this by calculating the stress distribution as a function of both x and y, applying equation (2.2) to get a resistivity distribution, and then using Maxwell's equations to calculate the predicted resistivity of the flexure. This was compared to observed experimental resistance results. The trends of the predicted and measured data were different and Johns concluded that Smith's model was insufficient for the bending case.

A qualitative examination can explain the discrepancy. If the beam in Figure 2.5 is reduced to two piezoresistive elements, one above and one below the neutral axes, the predicted response will be magnified and easier to examine. This assump-

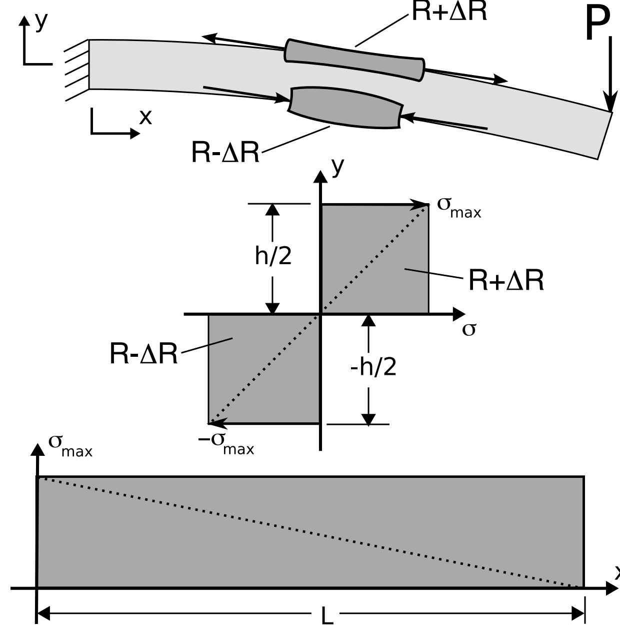

Figure 2.6: The unexpected nature of a bending flexure's piezoresistive response can be illustrated by approximating the beam as two parallel axially-loaded piezoresistors.

tion is shown in Figure 2.6, which also shows the distributed bending case in dotted lines for comparison. The lumped piezoresistor above the neutral axes is in tension, or positive stress resulting in a resistance of $R + \Delta R$. The lumped piezoresistor below the neutral axes is in compression, or negative stress resulting in a resistance of $R - \Delta R$. We know from equation (2.5) that for a lumped element in tension or compression

$$\Delta R = \pi_A \sigma_{max} R, \tag{2.6}$$

and the total resistance of the two parallel resistors is

$$\frac{1}{R_T} = \frac{1}{R + \Delta R} + \frac{1}{R - \Delta R}. \tag{2.7}$$

Combining equations (2.6) and (2.7) shows that the total resistance reduces to

$$R_T = \frac{R}{2} - \frac{(\pi_A \sigma_{max} R)^2}{2R}. \tag{2.8}$$

As shown by equation (2.8), the total resistance of the flexure, R_T, will always *decrease* as the maximum stress increases regardless of the sign of π_A. Correcting the assumptions from a lumped model to a more accurate distributed model will only reduce this response, but will not change the trend. Experimental results from flexures in bending contradict this prediction by *increasing* as the maximum stress increases.

2.4 Integrated Piezoresistive Sensing — Bending

We now develop a model describing the piezoresistive response to flexures in bending that accurately predicts behavior observed experimentally. We will continue to assume that shear and axial stresses may be neglected. In addition we will assume that the material is isotropic and that the cross section is constant along the length of the beam. Using these assumptions the piezoresistive effect can be reduced to some function of the bending stress defined at $y = h/2$ and $x \in [0, L]$.

The beam in Figure 2.5 is divided into n segments of length ℓ, such that $L = n\ell$, to capture the stress distribution in the x direction. The total resistance of the flexure is the sum of the segment resistances, and the total fractional change in resistance is

$$\frac{\Delta R_T}{R_T} = \frac{\sum_{i=1}^{n} R_i}{R_T}. \tag{2.9}$$

By defining r to be the initial resistance per unit length and the piezoresistive multiplier ϕ to be a function of the average maximum bending stress of the ith segment, $\sigma_{i,B}$, equation (2.9) becomes

$$\frac{\Delta R_T}{R_T} = \frac{\sum_{i=1}^{n} r\ell\phi(\sigma_{i,B})}{rL},$$

which reduces to

$$\frac{\Delta R_T}{R_T} = \frac{1}{n}\sum_{i=1}^{n} \phi(\sigma_{i,B}). \tag{2.10}$$

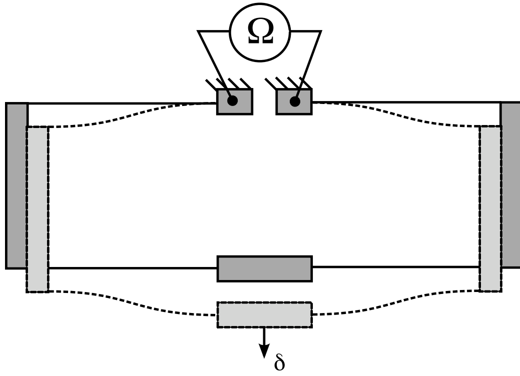

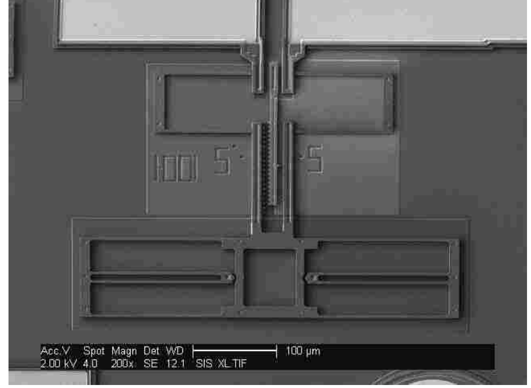

Figure 2.7: Piezoresistive coefficients for flexures under bending loads are determined experimentally using a test structure.

The results reported by Waterfall [21] imply a quadratic correlation between bending stress and resistance change. A quadratic function can always be positive, like the experimental results, and its curvature can capture the observed nonlinear response. Assuming ϕ is of the form

$$\phi(\sigma_{i,B}) = \pi_B \sigma_{i,B}^2, \tag{2.11}$$

where π_B is the empirically-determined bending piezoresistive coefficient, then equation (2.10) becomes

$$\frac{\Delta R_T}{R_T} = \frac{\pi_B}{n} \sum_{i=1}^{n} \sigma_{i,B}^2. \tag{2.12}$$

Figure 2.7 shows one of the devices that was used to measure the piezoresistive response to bending. Three devices were used, one with MUMPS poly1 flexures, one with poly2 flexures, and one with poly12 flexures. The resistance of the device is measured across its two anchor pads. Its displacement is measured using a vernier that is fabricated as part of the device. The vernier is accurate to 0.5 μm.

The flexures can be analyzed as a cantilever beam with the fixed end where the flexure connects to a rigid piece and the free end at the inflection point of the flexure. The equivalent cantilever displaces 1/4 of the total device displacement.

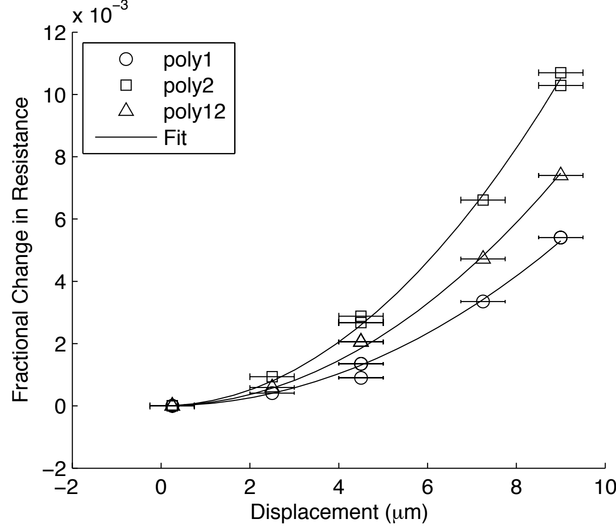

Figure 2.8: The piezoresistive response of flexures in bending follows a quadratic trend. This data was taken from devices such as the one shown in Figure 2.7.

Using small-angle assumptions, the maximum bending stress along the cantilever beam is

$$\sigma_B = \frac{3E\delta h}{2L^3}(L - x). \tag{2.13}$$

The brittle nature of polysilicon only allows displacement up to about 10% of the flexure length. As this is near the bounds of where small-angle linearization assumptions are valid, an elliptic integral solution is used as a check [27]. The stresses calculated using small-angle assumptions are within 1% of the elliptic integral solution.

The calculated bending stress profile and the experimental data are used to fit equation (2.12) by selecting an appropriate π_B for each fabrication layer. Figure 2.8 shows the experimental data points and their fits. The data fits the quadratic response of equation (2.12) to an R^2 value of 0.99 or greater. The bending piezoresistive coefficients for poly1, poly2, and poly12 are 1.8×10^{-9}, 3.5×10^{-9}, and 2.5×10^{-9} MPa^{-2}

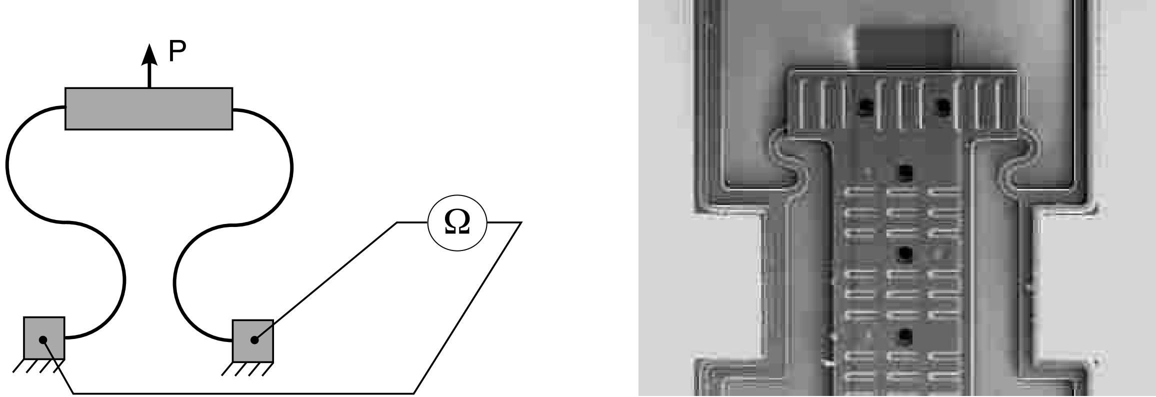

Figure 2.9: This structure has axial and bending stress components that are both significant.

respectively. This is an empirical model of the piezoresistive response to bending, just as Smith's model [8] was empirical.

2.5 Integrated Piezoresistive Sensing — Combined

The axial and bending piezoresistive models can be combined to predict the piezoresistive response of flexures to more complex loading conditions. The assumption of long, thin flexures where $L \ll h$ implies that shear forces are negligible. Given this assumption, all stress distributions for a long, thin flexure can be described as a superposition of axial and bending stresses.

The Piezoresistive Flexure Model (PFM) combines the piezoresistive response to both axial and bending stresses,

$$\frac{\Delta R}{R} = \frac{1}{n}\sum_{i=1}^{n}(\pi_A \sigma_{i,A} + \pi_B \sigma_{i,B}^2). \tag{2.14}$$

It is used just as the piezoresistive bending model— equation (2.12). The flexure being modeled is divided into n segments and the average axial and maximum bending stresses are calculated for each segment. The parameters π_A and π_B are orthogonal because they can be determined independently of each other as shown previously.

A structure using complexly loaded flexures was fabricated to validate the PFM. It consists of two S-curved flexures that are symmetrically joined at one end

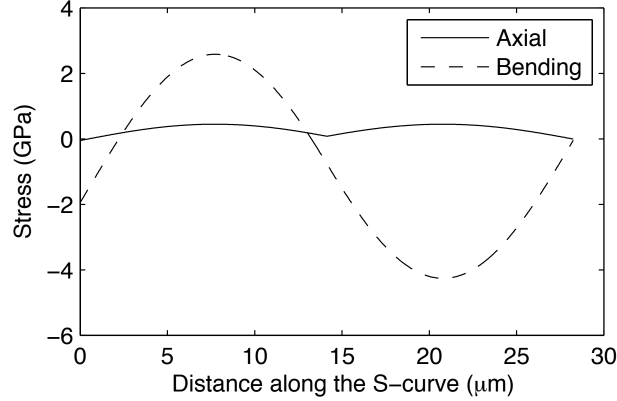

Figure 2.10: Finite-element analysis is used to model the axial and maximum bending stresses along one of the S-curve flexures of the device in Figure 2.9.

where a force can be applied, and anchored on their other ends. A schematic and image of the structure are shown in Figure 2.9. The curves along the flexures have a radius of 4.5 μm, an in-plane width of 3 μm, and an out-of-plane thickness of 2 μm. The flexures are fabricated from the MUMPs poly1 layer. The force is applied in the same manner that it was applied for the axial stress testing. The axial and maximum bending stresses along one of the S-curve flexures are shown in Figure 2.10 for an applied load of 2.5 mN. The stresses were calculated using commercial finite element code[2].

The predicted piezoresistive response is found by applying the PFM to the calculated stresses. The prediction is compared to experimental data points in Figure 2.11. The PFM prediction is within the accuracy of the experimental measurements. The error bars on the experimental data points represent the 95% confidence interval for the force applied to the structure. The force is applied using a force gauge such as the one shown applying force to the axial test structure in Figure 2.3. The uncertainty comes from force gauge displacement uncertainty, geometry variation,

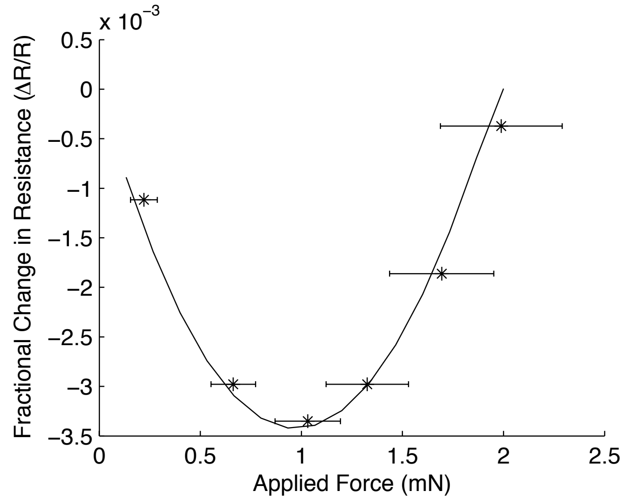

Figure 2.11: The predicted and measured piezoresistive response of the S-curve flexure device shown in Figure 2.9 matches well.

and material property uncertainty [25]. As the force gauge is deflected all of these factors contribute to the uncertainty of the force output.

2.6 Conclusion

Integrated piezoresistive sensing of MEMS devices is an effective way to produce small, reliable, accurate, and economical sensors to monitor compliant MEMS devices. While piezoresistive flexures do not respond to bending stresses in a way predicted by Smith's linear model, they do behave in a predictable and useable manner. Piezoresistive flexures follow a quadratic response to bending. The PFM combines Smith's linear model for axial loading with the observed quadratic response to bending stresses. Through this superposition the PFM can accurately model a flexure's piezoresistive response even under complex loading conditions. Using the PFM it is possible to design compliant MEMS devices that have integrated piezoresistive sensing.

[2]Using ANSYS BEAM3 elements the axial stress can be accessed through the ETABLE entry LS 1 and the bending stress through entry LS 2.

Chapter 3

A Self-Sensing Long-Displacement MEMS Device

3.1 Introduction

The Piezoresistive Flexure Model (PFM) can aid in the design of complex self-sensing compliant devices where critical components provide both mechanical functionality and system monitoring. It is important to consider both compliant-mechanism design to prevent failure, and piezoresistive design to maximize the sensing signal-to-noise ratio. Stresses must be accurately modeled when designing for the controlled deformation of compliant mechanisms. The PFM uses that stress information to predict the piezoresistive response. This coupled problem can then be optimized to produce an effective and useful MEMS device such as a self-sensing long-displacement device. This study describes the design of a MEMS device that is capable of displacements greater than 500 μm and produces a measurable signal that is proportional to its displacement. This design exercise is presented to demonstrate how integrated piezoresistive sensing can be incorporated into a useful compliant MEMS device.

Large-displacement MEMS devices have a variety of applications in areas such as component positioning, microassembly, robotics, biotechnology, and optics. These devices often have design challenges such as size, stability, reliability, and accuracy. Surface micromachined MEMS are typically fabricated from polycrystalline silicon, which is a brittle material, and the stress must be carefully controlled to reduce the risk of catastrophic failure of the flexure. This is a particular challenge where large deflections are required. It is possible to connect multiple small flexures in series and parallel to achieve the large deflections, but there is usually a compromise between size and stability for such a device [28].

At the macro scale, it is common to use rigid links, pin joins, and sliders to achieve large-displacement devices. Such methods are less effective for MEMS due to the limitations of planar fabrication processes, and the challenges associated with rubbing surfaces. Rubbing surfaces have a negative impact on reliability because the resulting friction produces wear, particle generation, and binding [29, 30]. In addition the joint clearances required cause uncertainty in the output displacement of the device.

For MEMS positioning applications it is usually critical to monitor the device displacement. It is possible to observe the device performance from "off-chip" using a microscope or a laser-doppler-vibrometer. However, very little has been reported on "on-chip" sensors that can measure MEMS displacements greater than 100 μm. On-chip displacement sensing is required for an economical solution to reliable, repeatable, and accurate positioning.

We will proceed to design a device with three design goals. It will achieve a linear displacement greater than 500 μm. It will constrain the motion to the desired direction by maintaining high off-axis stiffness. It will incorporate integrated piezoresistive sensing for on-chip displacement monitoring.

3.1.1 Piezoresistive contact-aided linear mechanism

A piezoresistive contact-aided linear mechanism is used to meet our design goals [31]. It is formed by supporting an output shaft between a set of rollers that act like linear bearings. As the shaft moves the rollers rotate allowing the shaft to translate without any rubbing parts, as shown in Figure 3.1. Additionally, the rollers rigidly constrain the motion parallel to the shaft.

Each roller maintains a no-slip condition via a pair of thin flexures that are wrapped around the roller. One connects the roller to the shaft and the other to kinematic ground. As the shaft translates and the rollers rotate, the flexures unwrap themselves along the shaft and the grounding anchor. This is illustrated in Figure 3.2.

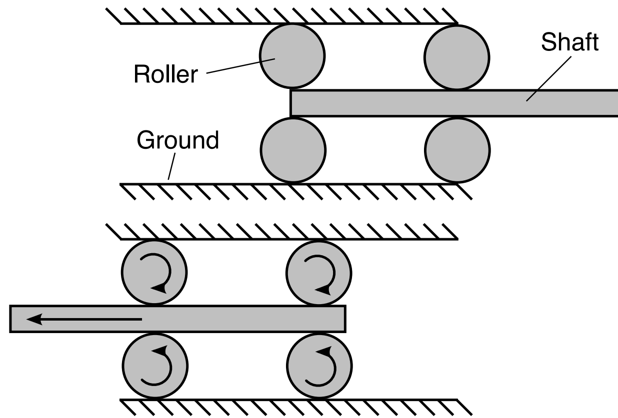

Figure 3.1: A rolling linear mechanism allows for rigidly constrained motion without any rubbing parts.

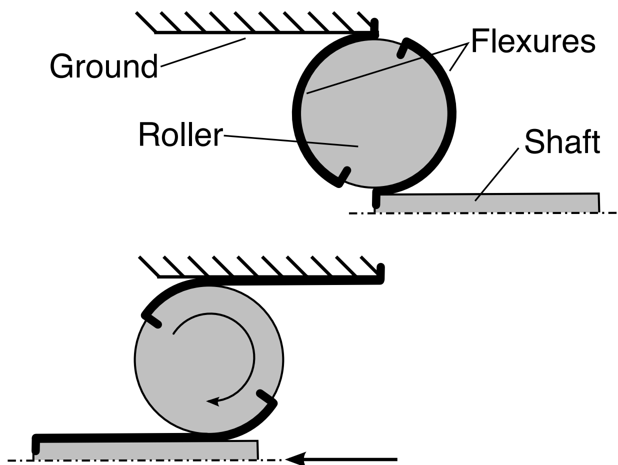

Figure 3.2: A no-slip condition is maintained as flexures that are wrapped around the rollers unwrap themselves along the shaft and the grounding anchor when the shaft moves.

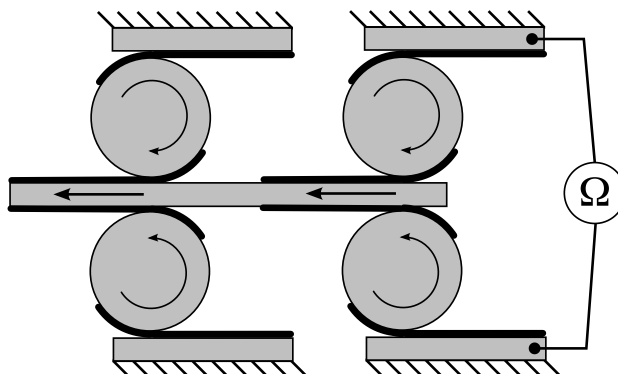

Figure 3.3: The structure is piezoresistive and changes resistance as the flexures are stressed during shaft motion.

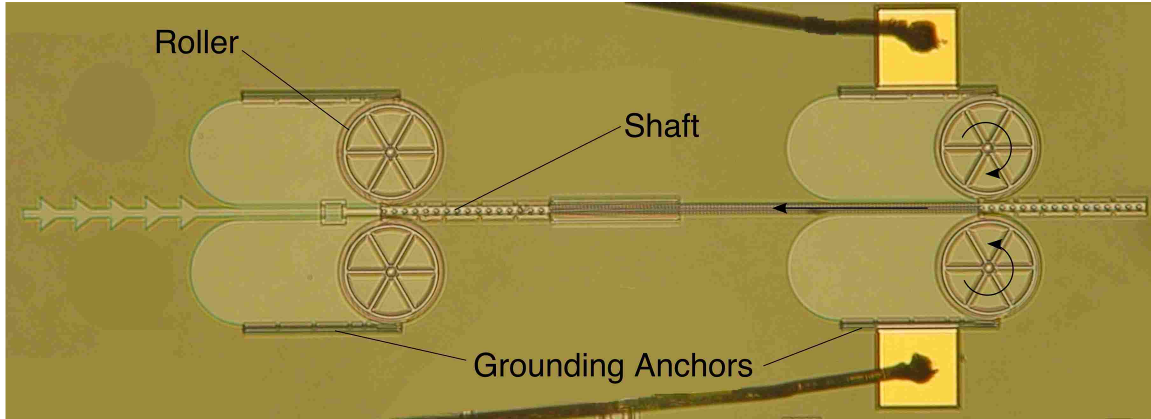

Figure 3.4: A light microscope image of a piezoresistive contact-aided linear mechanism.

Surface micromachined MEMS are often fabricated with highly doped polycrystalline silicon, which is piezoresistive. A piezoresistive structure exhibits a change in electrical resistance when it experiences mechanical stress. The flexures in this device form a current path connecting the grounding anchors. The resistance between the two ground anchors changes as the flexures unwrap. The result is an easily measurable phenomenon (resistance) that changes proportionally in response to the shaft output motion as shown in Figure 3.3. This gives the device its "self-sensing" capability.

Figure 3.4 shows an image, taken with a light microscope, of a piezoresistive contact-aided linear mechanism fabricated using the MUMPs process [6]. Combining this device with a long-displacement actuator (e.g., [32, 33, 34, 35]) will produce a system capable of automated, accurate, long-displacement positioning and manipulation.

3.2 Mechanical Design

Piezoresistive contact-aided linear mechanisms are able to displace large distances due to the constrained curvature of their flexures [31]. Given typical cantilever loading conditions a long thin polycrystalline-silicon flexure can only deflect up to approximately 10% of its length. However, a flexure that has its curvature constrained

all along its length, by conforming to a surface, can deflect much farther than 10% of its length. This is explained by examining the stresses of both flexures.

Assuming a linearly elastic, isotropic material, the Bernoulli-Euler equation for long thin flexures describes the moment at any location along the flexure as

$$M = EI\frac{d\theta}{ds}, \tag{3.1}$$

where E is the modulus of elasticity, I is the moment of inertia for the cross section, and $d\theta/ds$ is the curvature at the location s along the beam. The curvature is the inverse of the radius-of-curvature,

$$r' = \frac{1}{d\theta/ds}, \tag{3.2}$$

that is also a function of the location s along the length of the beam.

For a cantilever flexure, the minimum effective radius occurs at the fixed end as shown in Figure 3.5. The minimum radius of curvature implies the maximum bending stress. Once the maximum allowable stress is reached at the point of minimum radius, the flexure cannot deflect further without breaking. As shown in Figure 3.5, a flexure in contact with a support surface has the support surface's radius of curvature imposed upon its entire length. The result is that contact-aided flexures have a relatively uniform stress distribution and are able to achieve large deflections without failure.

The bending stress of a flexure is

$$\sigma_B = \frac{M(s)h}{2I}, \tag{3.3}$$

where h is the width of the flexure (parallel to its plane of deflection). From equations (3.1) and (3.2) we can define the moment as

$$M = \frac{EI}{r'(s)}. \tag{3.4}$$

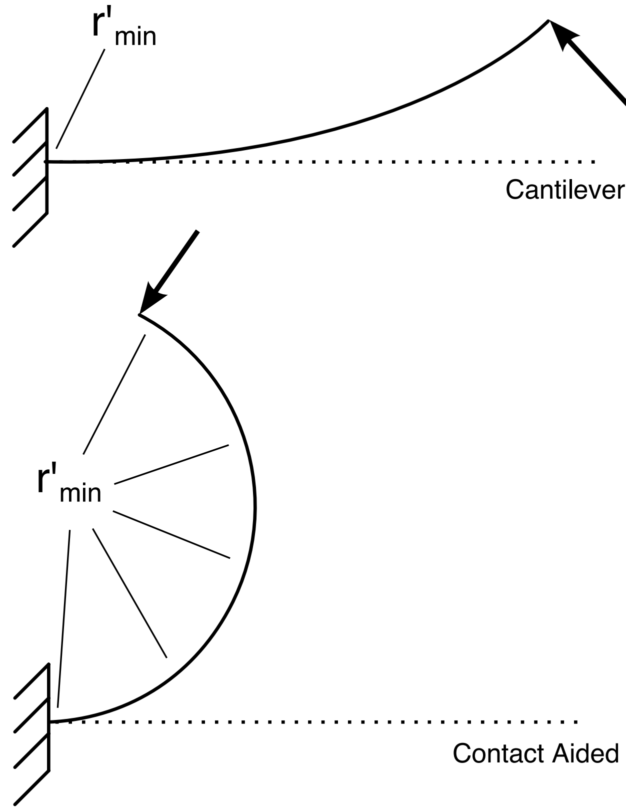

Figure 3.5: Cantilever flexures have their smallest radius-of-curvature (and therefore maximum stress) only at their fixed end. Contact-aided flexures can have their smallest radius of curvature along their entire length allowing for larger deflections.

The effective radius-of-curvature is a function of both the initial fabricated radius and the new radius imposed upon the flexure

$$r' = \left(\frac{1}{r_s} - \frac{1}{r_0} \right)^{-1}. \tag{3.5}$$

This assumes that the beams are thin so that the neutral axis is effectively coincident with the centroidal axis even for initially curved beams.

The piezoresistive contact-aided linear mechanism is fabricated with the flexure initially wrapped around the roller such that $r_0 = r$, where r is the radius of the roller. This allows the flexure to be "unwrapped" off the roller. If the long thin flexure was "wrapped" onto the roller it can easily experience large enough compressive stresses to cause it to buckle under the applied load. This buckling was observed in early prototypes of the design. The surface that the flexure is conforming to is flat

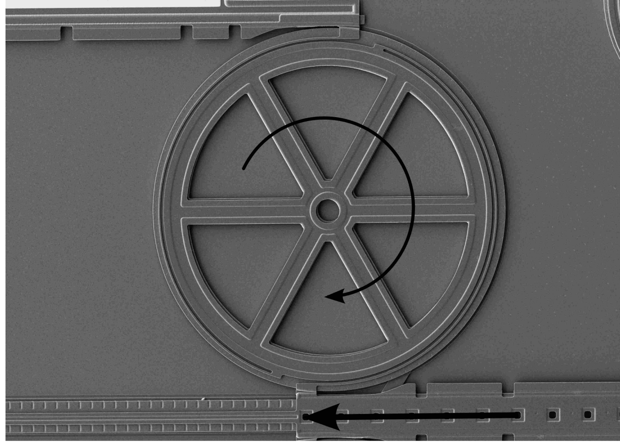

Figure 3.6: Scanning electron micrograph of a roller and its two flexures in their fabricated position.

such that $1/r_s = 0$. Equation (3.4) therefore becomes

$$M = \frac{EI}{r}. \tag{3.6}$$

Substituting equation (3.6) into equation (3.3) and rearranging gives the minimum radius for the rollers as

$$r_{\min} = \frac{Eh}{2\sigma_u}, \tag{3.7}$$

where σ_u is the ultimate strength of polycrystalline silicon. Assuming standard polycrystalline-silicon material properties, $r_{\min}$ is directly proportional to the flexure width, h. Using values of $E = 169$ GPa, $h = 2$ μm, $\sigma_u = 1.8$ GPa, and a safety factor of 1.5 yields a minimum roller radius of $r_{\min} = 140$ μm. $r_{\min}$ is independent of the out-of-plane thickness of the flexure.

A device was fabricated using these design values. Scanning electron micrographs of the device are shown in Figures 3.6 and 3.7 in both its fabricated position and a displaced position. This device is capable of shaft displacements up to 700 μm. The rollers' centers translate half the overall shaft displacement.

A close-up inspection of the deflected flexures reveal that they do not maintain a perfectly straight profile against the shaft or the anchor. This is shown in Figure 3.8 where it can be seen that the flexure bows away from its straight contact

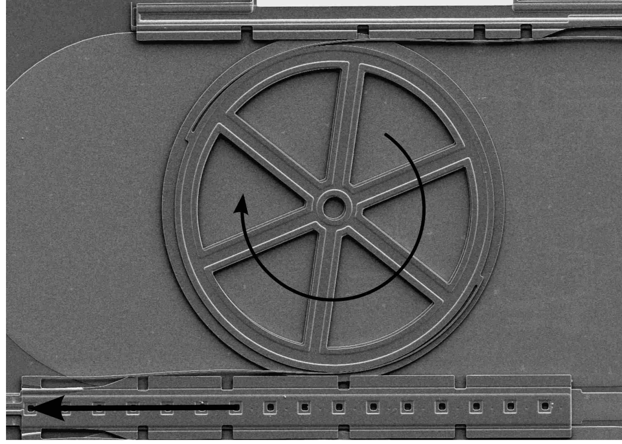

Figure 3.7: Scanning electron micrograph of a displaced roller and its two flexures conforming to the shaft and grounding anchor.

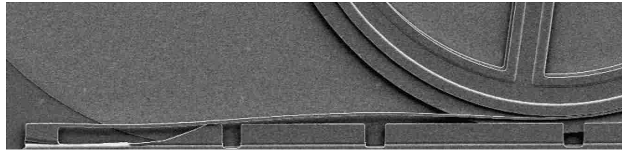

Figure 3.8: Scanning electron micrograph of a displaced flexure showing its non-ideal boundary conditions and the resulting deflection profile.

surface. Finite-element analysis of the flexure could not reproduce this bowing until the fabrication clearance allowance was included in the simulation. This clearance allowance is next to where the flexure is connected to the shaft or the anchor. It creates a region where the flexure is unsupported by the shaft or anchor. When this unsupported region is included in the finite-element analysis the flexure bowing is predicted. Fortunately, the maximum bending stresses along the flexure are affected by less than 1% compared to the ideal condition.

3.3 Piezoresistive Response

Polycrystalline-silicon flexures exhibit a well behaved, though unexpected, piezoresistive response [36, 37]. As shown in Chapter 2, the piezoresistive response of long thin polycrystalline-silicon flexures is a function of their axial and bending stresses,

$$\frac{\Delta R}{R} = \frac{1}{n}\sum_{i=1}^{n}\left(\pi_A\sigma_{i,A} + \pi_B\sigma_{i,B}^2\right). \tag{3.8}$$

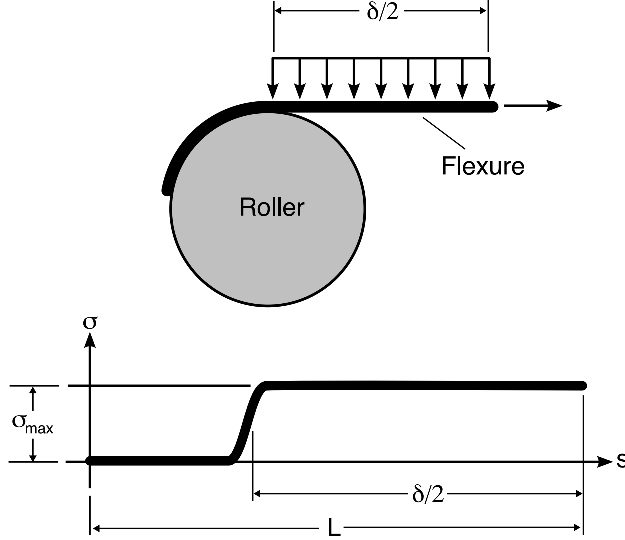

Figure 3.9: As the flexure unwinds onto the shaft or the grounding anchor the fraction of flexure that is stressed increases until the displacement (δ) is equal to double the length of the flexures.

$\Delta R/R$ is the fractional change in resistance of the flexure. n is the number of elements into which the flexure is subdivided. π_A and π_B are the axial and bending piezoresistive coefficients, which are determined experimentally. Finally, $\sigma_{i,A}$ and $\sigma_{i,B}$ are the axial and bending stresses of the ith element.

As demonstrated in the previous section, the stresses along the flexure are determined by its curvature. The axial stress is negligible. The bending stress transitions from zero to the maximum bending stress, σ_{max}, in the small length that is moving from the roller to either the shaft or the grounding anchor. As the displacement, δ, increases, so does the fraction of flexure that is stressed. The flexure is completely stressed when the displacement is equal to double the flexure length, $2L$. This is shown graphically in Figure 3.9.

The maximum bending stress is defined by rearranging equation (3.7) and setting r equal to the roller radius, such that

$$\sigma_{\max} = \frac{Eh}{2r}. \tag{3.9}$$

Equation (2.14) can be modified, neglecting axial stress and the portion of flexure that has zero bending stress resulting in

$$\frac{\Delta R}{R} = \frac{1}{n}\sum_{i=1}^{k} \pi_B \sigma_{i,B}^2, \tag{3.10}$$

where k is the closest integer to half the displacement divided by the flexure length and multiplied by the total number of elements,

$$k \approx \frac{\delta}{2L} n. \tag{3.11}$$

Substituting $\sigma_{\max}$ from equation (3.9) into equation (3.10) and pulling the constant parts out of the summation yields

$$\frac{\Delta R}{R} = \frac{\pi_B E^2 h^2}{4r^2 n}\sum_{i=1}^{k} 1,$$

which simplifies to

$$\frac{\Delta R}{R} = \frac{\pi_B E^2 h^2}{4r^2 n} k. \tag{3.12}$$

Substituting equation (3.11) into (3.12) yields

$$\frac{\Delta R}{R} = \frac{\pi_B E^2 h^2}{8r^2 L} \delta. \tag{3.13}$$

This indicates that the piezoresistive response should be a linear function of displacement. The slope of the response increases with increasing h, and decreases with increasing r and L. However, due to stress and geometry constraints, h, r, and L are coupled. h and the minimum r are related through equation (3.7), and L can be no larger than 1/2 the circumference of the roller minus any fabrication constraints.

3.3.1 Experimental results

The piezoresistive bending coefficient was determined by measuring the response of a device with known bending stresses and negligible axial stresses. The

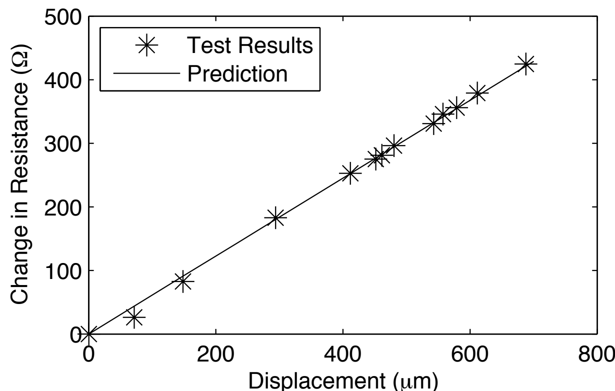

Figure 3.10: Predicted and measured piezoresistive responses match well showing a strong linear trend.

calibration device's response was fit to

$$\frac{\Delta R}{R} = \frac{1}{n} \sum_{i=1}^{n} (\pi_A \sigma_{i,A} + \pi_B \sigma_{i,B}^2)$$

setting $\sigma_{i,A}$ to zero (see Chapter 2, equation (2.14)). This calibration device was collocated with the test device to mitigate the effects of material property variation. The long-displacement device's piezoresistive response was calculated using equation (3.13). Setting π_B to 9.5×10^{-9} MPa^{-2}, E to 169 GPa, h to 2 μm, r to 140 μm, L to 40% of the roller circumference, and the initial resistance R to 32,700 Ω, gives the predicted piezoresistive response shown in Figure 3.10.

Also shown is a set of experimental test results for comparison. The experimental data points were taken by displacing the long-displacement device using microprobes. The displacement was measured optically by counting pixels from digital images giving a spatial resolution of about 1 μm. The device's resistance was measured at each displacement point. The prediction and experimental results match well as shown in Figure 3.10.

The experimental data shows that, for its displacement of 700 μm, this piezoresistive contact-aided linear mechanism has a linear response with a slope of 0.6 Ω/μm. The resistance was stable at each data point to 1 Ω, indicating a sensing resolution of about 2 μm.

3.4 Conclusion

Piezoresistive contact-aided linear mechanisms are compact MEMS devices that provide highly constrained, long-displacement linear motion. The motion is produced without any rubbing parts that could cause wear and hamper reliability. In addition, the device demonstrates a significant resistance change that is directly proportional to displacement making the devices "self sensing." In this study we have tested a device that has an output displacement of 700 μm with a sensing resolution of 2 μm.

A model has been presented that determines acceptable design geometry and predicts the piezoresistive response of the device. The device is well suited for applications that require controlled, large, on-chip displacements. The self sensing feature can be an important feature for feedback control of MEMS positioners. The resolution demonstrated with the prototype may be further improved for devices where higher accuracy is required. The geometry of the device can also be easily modified to create specific output displacements ranges for specific applications.

Chapter 4

Feedback Control of a MEMS Thermal Acutator

4.1 Introduction

Once a piezoresistive compliant device is obtained that performs the desired function and provides a strong sensing signal, it is possible to apply feedback control. This is a case study demonstrating the application of feedback control on a dynamically interesting system using a compliant piezoresistive structure as the feedback sensor.

Closed-loop feedback control of dynamic systems has been used for decades to improve system performance and reliability. Many researchers have applied feedback control to MEMS devices [38, 39, 12, 40, 41, 42, 43, 44, 45, 46]. One of the major challenges to the effective application of closed-loop control to MEMS is the feedback sensor. It is difficult to monitor the performance of many MEMS devices due to their micro-scale size. This paper presents a demonstration system composed of a thermal actuator mechanically coupled to a compliant piezoresistive structure. The changing resistance of the structure is used as the feedback sensor monitoring the thermal actuator's output displacement. This system demonstrates that compliant piezoresistive devices can produce high signal-to-noise ratio signals appropriate for feedback control, and that simple feedback control schemes can result in significant performance and reliability improvements for MEMS.

Some MEMS can be monitored through their output. For example, many optical MEMS produce an output that is easily observable [38, 47, 32, 48]. Other systems do not produce such macro-scale output. In some research environments an optical sensor such as a laser doppler vibrometer is used to measure small scale displacements for feedback control [12, 49].

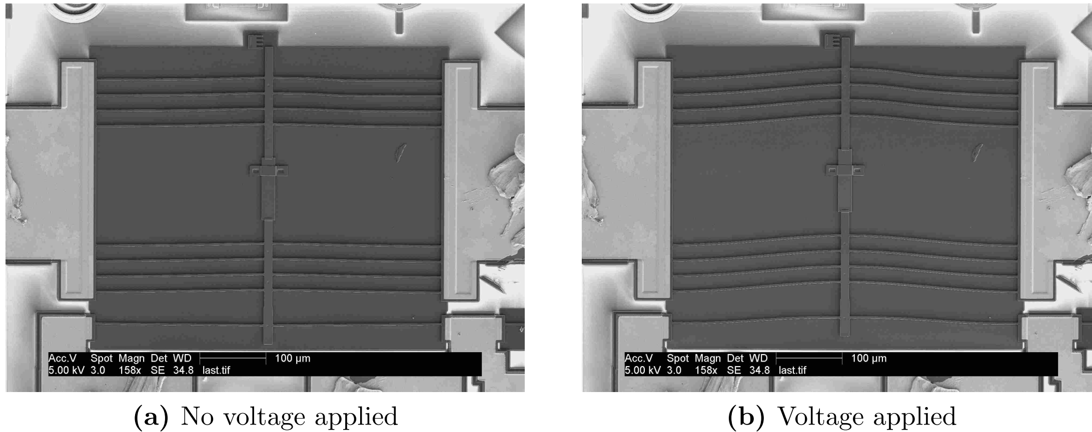

(a) No voltage applied **(b)** Voltage applied

Figure 4.1: Thermomechanical Inplane Microactuator (TIM) shown as fabricated and actuated.

The most common on-chip sensors are capacitive [12, 50, 43] or piezoresistive [1, 10]. Capacitive sensors are often problematic for surface micromachined devices because of the small surface areas for the sensing electrodes. The sensors therefore produce small changes in capacitance that are difficult to detect in the presence of parasitic capacitance [12]. The piezoresistive sensing utilized in this study differs from the traditional approach because no additional process step are required to create a piezoresistive region. Typically, on-chip piezoresistive sensing is achieved by selectively doping or depositing a piezoresistive current path in a region that experiences high compressive or tensile stress when the device displaces [51, 10, 52, 11]. The sensor in this study is a compliant device in which the entire structure is piezoresistive.

4.1.1 Piezoresistivity of polysilicon

The resistivity of a piezoresistive material is a function of the stress it is experiencing. For semiconductors, the piezoresistive effect is large — up to two orders of magnitude larger than for metals [8]. The piezoresistive properties of polycrystalline silicon are well documented [19] and form the basis for a variety of MEMS sensors such as accelerometers [22, 23] and pressure sensors [10, 24].

As stated earlier, the typical method for employing piezoresistivity in MEMS devices is to use additional process steps to selectively dope or deposit specific piezoresistive regions on the device. Those doped regions become isolated piezoresistive elements that ideally monitor the strain of the most stressed parts of the device. However, it is common to fabricate MEMS by patterning uniformly doped polysilicon layers[1]. By carefully designing the device to form a current path through its compliant flexures, which are fabricated from these uniformly doped polysilicon layers, the sensing functionality is integrated into the entire device. This is referred to as integrated piezoresistive sensing because it does not require attaching a separate sensor through selective doping.

4.1.2 Thermomechanical inplane microactuator

The Thermomechanical Inplane Microactuator (TIM) is an actuator that amplifies thermal expansion to produce a linear output force in the plane of the substrate [53, 54, 55, 56, 35, 57, 58]. It is constructed by suspending a shuttle off of the substrate with two symmetric arrays of thin beams. These beams are inclined in the direction of desired displacement in a bent-beam or chevron shape. The beams are attached to bond pads which are anchored to the substrate as shown in Figure 4.1a.

A voltage is applied across the two bond pads, which induces a current through the thin beams. The current generates ohmic heating, and as the temperature of the beams rise they expand. The lengthening of the beams causes them to buckle, and this buckling displaces the shuttle in the desired direction as shown in Figure 4.1b. The geometry of the TIM causes the small increases in beam length to be amplified into relatively large displacements of the center shuttle.

The TIM has many characteristics that make it a good choice for a variety of MEMS applications. The TIM's robust, reliable operation is realized through simple geometry that can be fabricated in a single layer. It produces large output forces and displacements from a small footprint and low input voltages [1, 53, 59, 54, 60, 61].

[1]Standard surface micromachining processes such as MUMPs [6] and SUMMiT [5] use uniformly doped polycrystalline layers.

The high output force and displacement characteristics of thermal microactuators make them ideally suited to meeting the actuation requirements of compliant bistable devices [53, 61, 62, 63]. They have also been used to power variable optical attenuators [64, 48], and RF switches [65, 66]. Additionally, thermal actuators have been shown to be a stable and repeatable actuator for MEMS nanopositioning applications [67]. The physics of thermal actuator operation are well understood with accurate and accessible models available to aid in device and control design [15, 57, 58, 56].

The TIM used in this study was fabricated using the MUMPs MEMS prototyping process [6]. The beams and shuttle are made in the poly1 and poly2 layers laminated together. This maximizes the available beam aspect ratio thus inhibiting out-of-plane motion. A poly0 structure is used under the TIM to mitigate stiction. The expansion beams are 250 μm long, 3 μm wide (in-plane), 3.5 μm thick (out-of-plane), and angled by 0.7 degrees.

Simplified mathematical models of thermal actuators using lumped elements and constant thermal properties do not generally match well with experimental data [58, 56]. The high temperature gradients that enable thermal actuators to work require that an accurate model incorporate temperature-dependent thermal and electrical properties. The long thin expansion beams also require a distributed solution to the thermal simulation. Given this nonlinear distributed problem, finite-difference [56] or finite-element [57, 68] solutions are appropriate.

An examination of the finite-element simulation for this TIM predicts a safe maximum displacement of about 10 μm. It also predicts a 400 Hz bandwidth for the thermal response. This is orders of magnitude below the mechanical natural frequencies reported by Hickey and Messenger [58, 68] which are around 100 kHz.

4.2 Piezoresistive Microdisplacement Transducer

The piezoresistive microdisplacement transducer (PMT)[14] used in this study utilizes a sensing flexure pair that is similar to the beam pairs of the TIM. The flexure pair is fabricated identically to a TIM beam pair, except that it is inclined

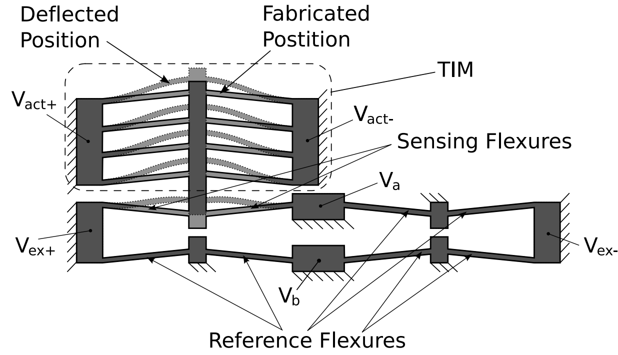

Figure 4.2: Physical schematic of the TIM/PMT setup.

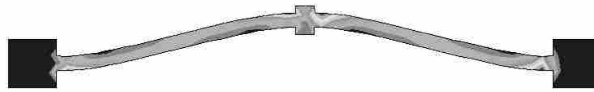

Figure 4.3: Finite-element-analysis displaying the stress distribution of PMT sensing flexures as they are displaced toward the top of the page.

in the opposite direction. Figure 4.2 illustrates the TIM/PMT layout, and how it functions. As the flexure pair is displaced it experiences increasingly greater stresses as shown in Figure 4.3. As a result of its inherent piezoresistivity, the sensing flexures' electrical resistance increases as the stress increases. The sensing flexures along with three fixed reference flexure pairs form the legs of a Wheatstone bridge as shown in Figure 4.4. The output of the bridge is the electric potential difference between V_a and V_b, which is a function of the bridge excitation voltage (V_{ext}) and the resistances of the bridge legs (flexure pairs). The result is that the displacement of the TIM can be inferred from the output voltage of the PMT. A scanning electron micrograph (SEM) of the TIM and PMT is shown in Figure 4.5. The PMT's initial resistiance is 2.4 kΩ. The sensor uses 3.7 mW when using a 3 V excitation across the bridge.

Using reference flexures in the Wheatstone bridge not only allows for a well balanced bridge, but also provides thermal compensation. The temperature profile of the PMT can be modeled the same way a thermal actuator is modeled. Heat transfer models that have been developed for MEMS thermal actuators [69, 56, 57, 68] show that the temperature profile of a long thin beam with current running through it is

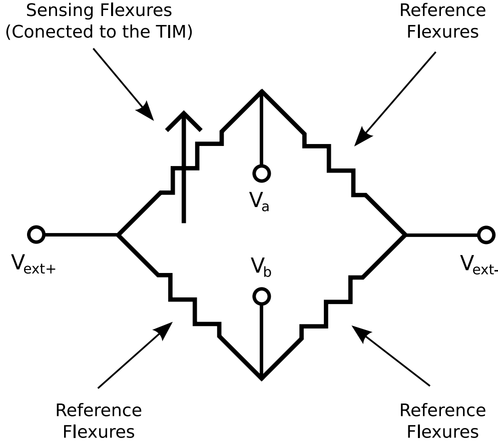

Figure 4.4: Electrical schematic of the PMT.

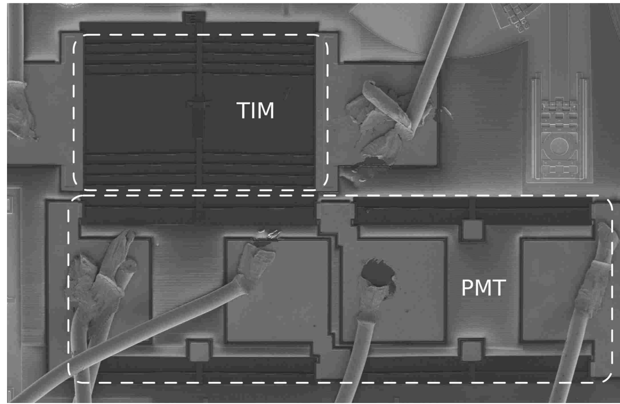

Figure 4.5: SEM of the TIM/PMT setup.

dominated by the internal ohmic heat generation and the large thermal sink of the substrate that is in close proximity to the beam. Therefore, the close proximity of the TIM to the PMT is not likely to affect the PMT's operating temperature. Any temperature changes are predominantly due to ohmic heating from the excitation voltage and will affect the sensing flexure pair and the three reference flexure pairs equally. Thus the Wheatstone bridge output voltage is effectively temperature independent.

With a 3 V excitation the PMT outputs approximately 1 mV per μm of displacement. To remove any common-mode interference from the TIM actuation

voltage, the Wheatstone bridge was excited using a floating power supply and the output voltage was measured using an instrumentation amplifier. Additionally, the signal was amplified further to a more convenient range and low-pass filtered with a 37 kHz second-order Butterworth filter. Unless otherwise noted, all of the data reported reflect this signal conditioning.

The PMT does require a significant force to displace. FEA modeling of the structure, including thermal expansion forces, predict that 15 μN are required to displace the PMT 5 μm. A TIM with these dimensions can provide approximately 300 μN at that displacement [70]. The PMT does not significantly alter the dynamics of the TIM. TIM dynamics are dominated by the heat tranfer dynamics of the thermal expansion beams, and the heat transfer of the expansion beams is not significantly affected by proximity to the PMT.

4.2.1 Piezoresistive response of the PMT

Doping concentrations for MUMPs are not controlled well. They are typically about 10^{19} phosphorus atoms/cm^3. Even though the exact piezoresistive response cannot be calculated, it is desirable to predict the general form of the response. From the piezoresistive flexure model described in Chapter 2, we know that the fractional change in resistance for a long thin polysilicon beam is

$$\frac{\Delta R}{R} = \frac{1}{n} \sum_{i=1}^{n} (\pi_A \sigma_{i,A} + \pi_B \sigma_{i,B}^2), \tag{4.1}$$

where n is the number of elements the beam is subdivided into, π_A is the axial piezoresistive coefficient, π_B is the bending piezoresistive coefficient, $\sigma_{i,A}$ is the axial stress for the ith element, and $\sigma_{i,B}$ is the maximum bending stress for the ith element. The fractional change in resistance is a function of the axial and bending stress along the entire length of the flexure.

The Wheatstone bridge output is a function of the fractional change in resistance

$$V_{out} = \frac{\Delta R/R}{4 + 2\Delta R/R} V_{ext}. \tag{4.2}$$

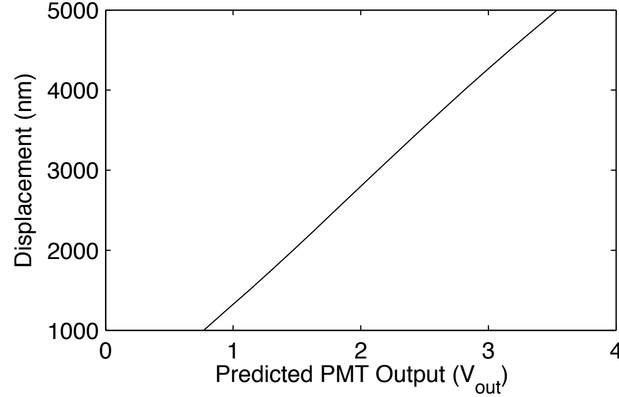

Figure 4.6: Predicted PMT output versus TIM displacement as calculated using the piezoresistive flexure model.

The Wheatstone bridge output is simulated by first calculating the axial and bending stresses using finite-element analysis. The axial stresses are about ten times as large as the bending stresses, and are significantly effected by the thermal expansion of the flexures which result from the bridge excitation voltage V_{ext}. The stresses are used in equation (4.1) to calculate the fractional change in resistance for various displacements of the PMT. The values -122.6×10^{-6} MPa^{-1} and 2.5×10^{-9} MPa^{-2} were used for π_A and π_B respectively because they are representative of piezoresistive coefficients for the MUMPs process as reported in Chapter 2. The fractional change in resistance is then used in equation (4.2) to predict the output bridge voltage. A negative excitation voltage is used to get the sensor response to increase with increasing TIM displacement. The predicted PMT output versus TIM displacement is shown in Figure 4.6. The piezoresistive flexure model predicts a nearly linear response for the PMT for an average flexure temperature of 325° C above ambient. This provides and approximation of what the PMT piezoresistive response will be. The slope of response is affected by what the piezoresistive coefficients will be for each particular fabrication run. The curvature is affected by the temperature profile of the beam.

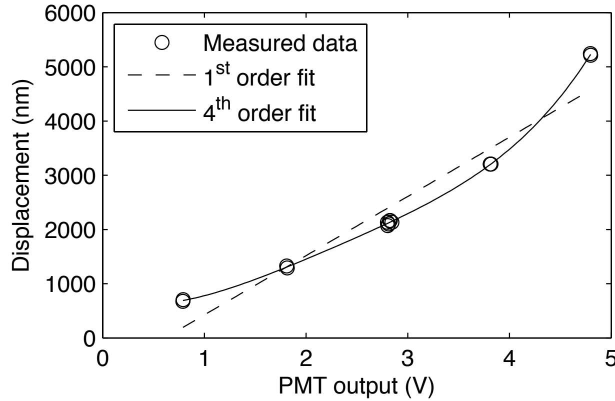

Figure 4.7: PMT output versus TIM displacement with the resulting first and fourth order regression lines.

4.2.2 Sensor characterization

The PMT is useful as a sensor because it has a specific and repeatable relationship between its resistance and its displacement. This relationship is a one-to-one mapping function such that a unique PMT output voltage corresponds to a unique displacement. To calibrate this particular TIM/PMT system, TIM displacements were measured and compared with the resulting PMT output voltages to characterize the PMT voltage-to-displacement mapping function. The displacements were measured by taking digital images of the deflected structure using a light microscope at 1000X magnification. Fiducial marks were integrated into the structure that facilitated sub-pixel measurement of the images by an image processing algorithm [15].

The measurement uncertainty and the device operation variability preclude an exact measurement of the displacement-to-voltage mapping, but it can be bound by a tight envelope. The envelope, a two dimensional region that has a 95% certainty of encompassing the mapping function, is determined using regression analysis to minimize the area of the envelope. Significant curvature was expected from previous experience, therefore data points were taken, in random order, at five evenly spaced levels to capture up to fourth-order curvature. A fourth-order fit was chosen to tightly bound the behavior of the system, thus allowing an accurate measurement of the system's noise. While the predicted response is close to linear, a fourth-order

fit will capture all the significant curvature such that any deviation from the fit will be measurement uncertainty. Sufficient replication was used (14 total data points) to quantify the uncertainty of the regression. Figure 4.7 shows the data points, a first-order linear fit ($R^2 = 0.9224$), and a fourth-order polynomial fit ($R^2 = 0.9997$). The regression's uncertainty is too small to illustrate clearly in the figure, but the maximum spread of the bounding envelope is ±110.4 nm. The resulting fourth-order regression relating PMT sensor output, V_{PMT}, in signal conditioned volts, to TIM displacement, δ_{TIM}, in nm, is

$$\begin{aligned} \delta_{TIM} = \; & 761.0 \ldots \\ & -(644.0)V_{PMT} \ldots \\ & +(883.8){V_{PMT}}^2 \ldots \\ & -(250.8){V_{PMT}}^3 \ldots \\ & +(28.1){V_{PMT}}^4. \end{aligned} \quad (4.3)$$

TIMs have demonstrated significantly better positioning repeatability than ±110.4 nm [67]. Additionally, the physics governing PMT operation imply a well behaved, continuous function mapping displacement to stress to resistance change. It is therefore reasonable to assume a majority of the ±110.4 nm uncertainty comes from the optical displacement measurements. We can also assume that the slope of the PMT mapping function is bound inside the envelope defined by the regression.

The linear fit, shown in Figure 4.7, approximates the average slope of the PMT mapping function. The measured noise from the PMT output can be transformed into sensor repeatability using variance propagation on the linear fit. The sample with the largest spread had a standard deviation of 4.3 mV that maps to a spread having a standard deviation of 4.7 nm, or a 95% confidence interval of ±9.1 nm. In other words, a PMT measurement is within 9.1 nm of another PMT measurement that has the same output voltage. Additionally, the PMT output voltage indicates the absolute position to within 110.4 nm.

The same regression study was performed in a scanning electron microscope[2] (SEM) to facilitate finer precision displacement measurements. The same image processing algorithms were used on images with 7500X magnification. The vacuum environment inside the SEM significantly changes the heat transfer physics of the sensor and the actuator, resulting in greater PMT sensitivity. As a result, a smaller signal conditioning gain was required. The electrical environment inside the SEM is also noisier, requiring a more aggressive lowpass filter. Figure 4.8 shows the data taken in the SEM, a first-order linear fit ($R^2 = 0.9890$), and a fourth-order polynomial fit ($R^2 = 0.9998$). Once again this regression defines an envelope that has a 95% certainty of containing the actual PMT mapping. Using the SEM for displacement measurements reduces the envelope's spread to ±43.8 nm. The sensor repeatability, when operated in the SEM, is ±11.6 nm as calculated from a variance propagation just as was done with the optical results. The degraded repeatability likely results from the noisy electrical environment inside the SEM. The fourth-order regression relating PMT sensor output, signal conditioned for the SEM, to TIM displacement, in nm, is

$$\begin{aligned} \delta_{TIM} &= 275.7 \ldots \\ &+(268.9)V_{PMT} \ldots \\ &+(321.7){V_{PMT}}^2 \ldots \\ &-(65.9){V_{PMT}}^3 \ldots \\ &+(6.1){V_{PMT}}^4. \end{aligned} \tag{4.4}$$

4.2.3 Dynamic performance

Figure 4.9 is a plot comparing TIM input voltage and the resulting PMT output voltage. The square wave input reveals a 10% to 90% rise time of 500 μs, matching expectation for the rise time of this TIM [16, 68, 57]. The sinusoidal input demonstrates the expected double frequency TIM response. The double frequency response is a result of the TIM physics. The TIM output displacement is a function

[2]Philips XL30 ESEM FEG

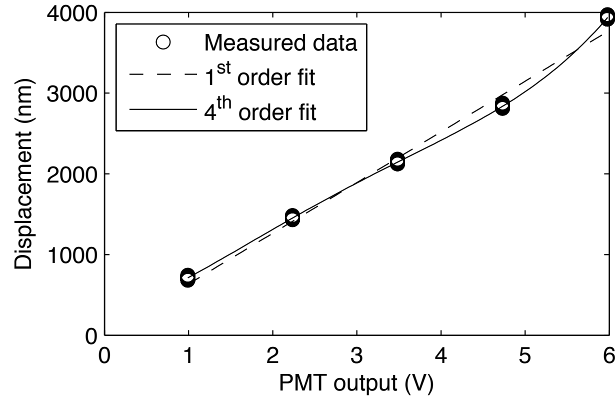

Figure 4.8: PMT output versus TIM displacement with the resulting first and fourth order regression lines. Data taken in the vacuum environment of an SEM.

of the expansion beam temperature, which is a function of the power into the system. The power is proportional to the input voltage squared. The trigonometric identity

$$\sin^2 x = \frac{1 - \cos 2x}{2} \tag{4.5}$$

demonstrates that a squared sinusoidal input results in a vertically shifted, double frequency response. An intuitive description is that the TIM will actuate the same direction regardless of the voltage polarity.

Figure 4.9 also shows that the PMT produces a strong signal with low noise. The signal to noise ratio is 450 as measured by comparing a 95% confidence interval of the signal to its magnitude. The piezoresistive sensing phenomenon comes from the polysilicon band-gap energy responding to the changing inter-atomic spacing of the stressed crystalline structure. The dynamics of this phenomenon are much faster than the heat transfer dynamics of the system, or even the mechanical resonance of the device. It can therefore be assumed that the PMT does not contribute any dynamics to the output signal. The spike that is evident at the rising edge of the square wave is an electrical artifact . The spike happens too fast to be a physical effect of the system, and is still evident when a "dummy" system is used that has the same electrical layout without any piezoresistive output. The phenomenon is most

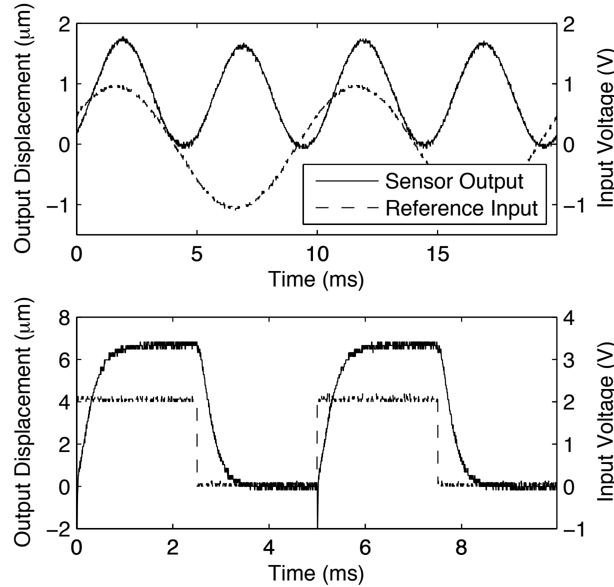

Figure 4.9: Plots comparing the input voltage to the TIM and the resulting output voltage of the sensor.

likely parasitic capacitive coupling between the Wheatstone bridge output and the input signal to the TIM, and will be explained in greater detail in the next section.

The frequency response of the TIM/PMT system was measured to facilitate control design. Figure 4.10 shows the frequency response as measured by a spectrum analyzer connected to the TIM/PMT system. The system was driven by a sine sweep with a signal that ranged from 0 to 3 V. Biasing the input to include only positive voltages avoids the nonlinear effects of the frequency doubling response shown in Figure 4.9. The validity of using a frequency response such as this one is confirmed by coherence values of 0.997 or greater throughout the frequency range measured.

The steep magnitude drop off at about 500 Hz results from the heat transfer dynamics of the TIM , and is close to the expected value of about 400 Hz that is reported in the literature [56, 57, 68]. The magnitude rise after about 5,000 Hz is likely due to parasitic capacitance between the Wheatstone bridge and the input signal to the TIM.

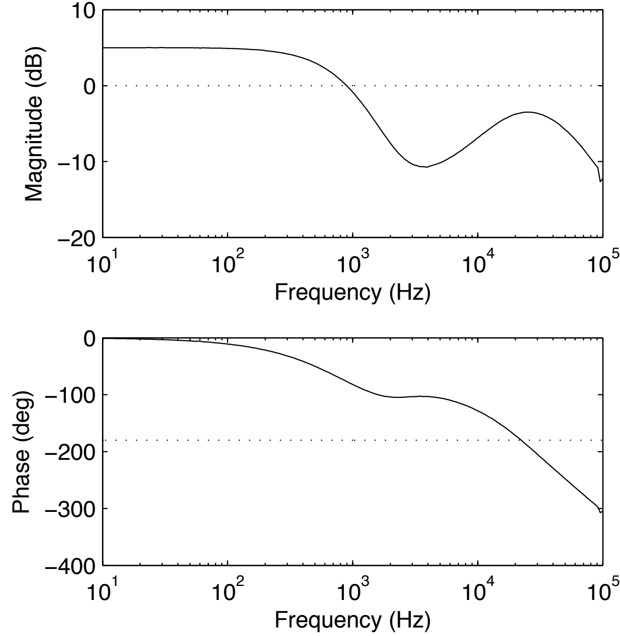

Figure 4.10: Open-loop freqency response of the TIM/PMT system.

4.2.4 Parasitic capacitance

A low-order approximation of the thermal and electrical dynamics of the system provide greater confidence that parasitic capacitance is being observed. In addition it provides some insight into how to minimize the problem. The primary contribution to the output signal from the PMT is TIM motion. Our hypothesis is that a secondary, smaller contribution comes from parasitic capacitance. While it does not capture the distributed effects of TIM heat transfer dynamics [56, 57, 68], a first-order lumped model of the actuator provides a reasonable approximation of its behaviour and allows the effects of parasitic capacitance to be analyzed. A typical first-order transfer function with a time constant of 300 μs can be used to model the dynamic behavior of the TIM:

$$\frac{V_{out}}{V_{Act}} = \frac{1}{\tau s + 1}. \tag{4.6}$$

Parasitic capacitance is also a significantly distributed phenomenon. The PMT structure is capacitively coupled to the TIM, the surrounding environment, and nearby

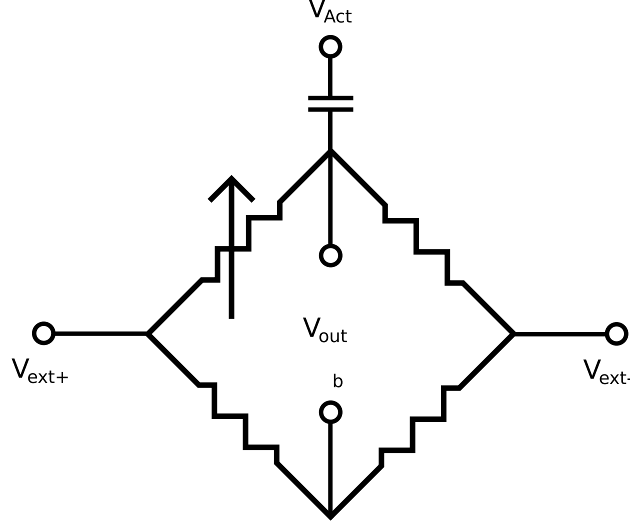

Figure 4.11: A schematic describing the low-order lumped model of parasitic capacitance between the PMT and the TIM actuation voltage.

electrical connections. Once again we will use a first-order lumped approximation to investigate how parasitic capacitance affects the PMT output dynamics. The parasitic capacitance is modeled by connecting one output terminal of the PMT Wheatstone bridge to the TIM actuation voltage, V_{Act}, through a representative parasitic capacitor, C, as shown in Figure 4.11. The corresponding transfer function relating V_{Act} to V_{out} is

$$\frac{V_{out}}{V_{Act}} = \frac{Cs}{Cs + 1/2}. \tag{4.7}$$

The parasitic capacitance acts in parallel with the actuator dynamics on the output of the sensor. In other words, the TIM actuation voltage has two paths to contribute to the PMT output dynamics. The desired transmission is the actuation voltage causing TIM motion, and that motion being measured by the changing resistance of the sensing flexures. The undesirable transmission is through the parasitic capacitance. The system dynamics can be estimated by combining the low-order approximations of these two sources of dynamics in parallel as shown in Figure 4.12. A low-pass filter is applied to the sensor output signal, as was done in the experimental system. The resulting frequency response is of the same form as the measured

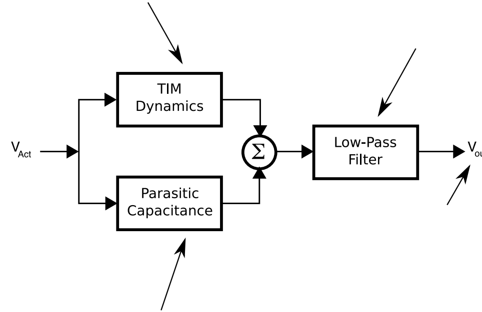

Figure 4.12: Schematic showing the sources of dynamics reflected in the sensor output.

response shown in Figure 4.10. This leads us to believe that parasitic capacitance causes of the high-frequency rise in magnitude observed in the experimental system.

Experience also shows that both the spikes evident on the step response and the high frequency rise in magnitude on the frequency response are mitigated by reducing the effective value of the parasitic capacitor. Isolating the electrical connections and putting grounded structures between the TIM and the PMT both reduce the phenomenon. While this parasitic capacitive phenomenon does not represent TIM motion, it does have an effect on system closed-loop stability and control design.

4.3 Control Design

The empirical frequency response shown in Figure 4.10 is used to design standard control laws for the TIM/PMT system. We will use the empirical data for control design because it captures accurate information about the system without having to model the distributed thermal and electrical dynamics.

The control designs described below follow the standard form shown in Figure 4.13 where $D(s)$ represents the controller dynamics and $G(s)$ represents the system dynamics including the actuator, sensor, and signal conditioning.

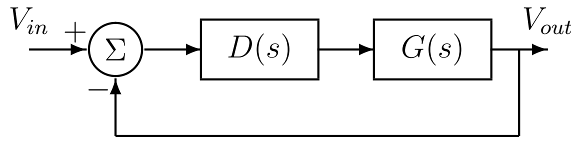

Figure 4.13: Feedback control (closed loop) block diagram.

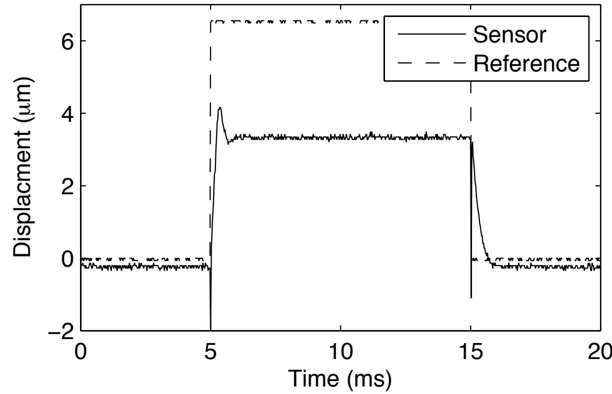

Figure 4.14: Proportional-control step response.

4.3.1 Proportional control

The open-loop frequency response in Figure 4.10 indicates that significant transient response improvement can be achieved with simple proportional control

$$D(s) = k_p. \tag{4.8}$$

The gain (k_p) can be increased to improve tracking performance until the high-frequency electrical artifact begins causing stability problems.

Figure 4.14 shows the decreased response time of the TIM under proportional control. The rise time with proportional control was 120 μs compared to 500 μs for open loop control.

While proportional control produces significant improvement for the transient response, it results in steady-state error. The steady state error results from the heat transfer physics of the system and is expected [15].

4.3.2 Integral-lead control

The steady-state error evident in the proportional control response is eliminated by an integrator in the control law. In addition, some form of derivative based dynamic control can effectively mitigate the negative effects an integrator has on the transient response. An integral-lead controller,

$$D_{i\ell}(s) = k\frac{s+\omega_z}{s(s+\omega_p)}, \tag{4.9}$$

is formed from a lead controller modified to include integration by increasing the order of the denominator. The lead portion of the control can be tuned so that it does not amplify the high frequency electrical artifact shown in Figure 4.10.

The integral-lead controller is implemented using a single op-amp stage as shown in Figure 4.15. The circuit parameters are related to the control values by the expressions

$$k = \frac{R_2}{L_1}, \tag{4.10}$$

$$\omega_z = \frac{1}{R_2C_2}, \tag{4.11}$$

and

$$\omega_p = \frac{R_1}{L_1}. \tag{4.12}$$

The control values were selected [71], using the open-loop frequency response (Figure 4.10), to set the controller zero (ω_z) to 200 rad/s, the pole (ω_p) to 10,000 rad/s, and the gain (k) equal in magnitude to the pole. These values were chosen as a compromise between rise time and overshoot. The predicted open-loop response, of the system with integral-lead control, has a gain margin of 1.8 and a phase margin of 45 degrees.

Figure 4.16 demonstrates the close tracking performance achieved with integral-lead control. No steady state error is evident, and the rise time is 190 μs, which is close to the performance achieved with proportional control.

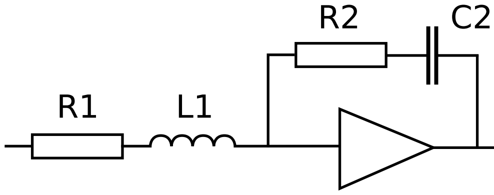

Figure 4.15: Schematic of integral-lead control implementation.

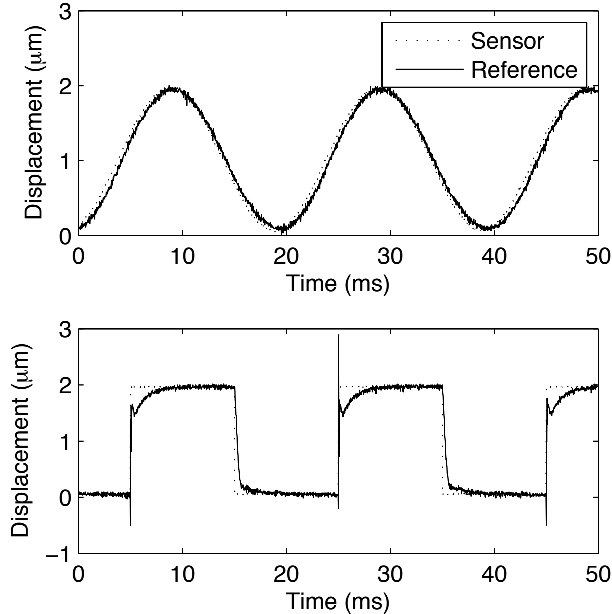

Figure 4.16: Integral-lead control tracking performance.

4.3.3 Steady-state control in a vacuum

Steady-state nanopositioning tests were run inside an SEM to provide a more accurate measurement of TIM displacement and to characterize its precision and repeatability. The vacuum environment inside the SEM slows the heat transfer dynamics of the TIM because there is no surrounding atmosphere through which heat can be conducted to the substrate [56, 15]. Additionally, the more aggressive low-pass filter with a 20 Hz roll-off frequency is required inside the harsh electrical environment of the SEM. The slower TIM dynamics, and the aggressive low-pass filter introduce instability when using the integral-lead control. However, a simple proportional integral control,

$$D(s) = k_p + \frac{k_i}{s}, \tag{4.13}$$

is sufficient because we are bandwith limited to 20 Hz by the roll-off frequency of the aggressive low-pass filter we used to compensate for the noisy electrical environment inside the SEM.

4.3.4 Position control results

TIM positioning accuracy was quantified by measuring the displacement resulting from five input voltage levels. Once again the data was taken in random order and with sufficient replication to measure uncertainty. Regression analysis was used to identify an envelope that bounds, to a 95% confidence, TIM displacement as a function of input voltage. Figures 4.17 and 4.18 show the open and closed-loop data points and their respective 4th order regressions. The open and closed-loop regressions have R^2 values of 0.9996 and 0.9998 respectively.

Although the analysis is similar to that done on the regressions in Figures 4.7 and 4.8, this analysis relates displacement to the *input* voltage driving the *system*. The previous analysis related displacement to the *output* voltage of the PMT.

The spread of the bounding envelopes are a measure of the uncertainty in the experiment. Potential uncertainty comes from input voltage variation, displacement measurement, and device operation variability. Implementing feedback control affects the device operation while the input voltage and the displacement measurement remain the same. Comparing the spread of the bounding envelopes for the open and closed-loop data sets reveals any significant effect feedback control has on TIM positioning accuracy.

The open-loop data is contained by an envelope with a maximum spread of ± 29.9 nm while the closed-loop data is bounded by an envelope with a maximum spread of ± 29.4 nm. These values are close to each other indicating that the sensor did not introduce significant noise that would degrade the system accuracy. Displacement measurements taken on a device that was known to not be moving isolated the uncertainty in the SEM measurement process. The SEM measurements have a 95% confidence interval of ± 23.1 nm. As this represents over 75% of the open and closed-

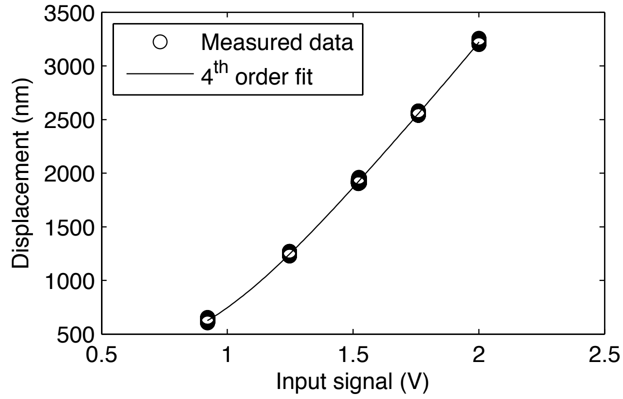

Figure 4.17: Open-loop nanopositioning data and regression.

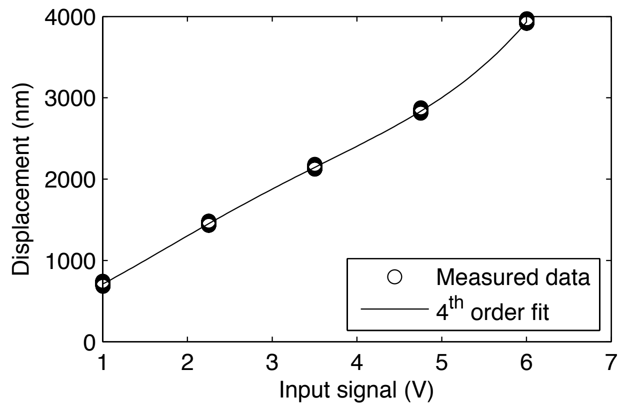

Figure 4.18: Closed-loop nanopositioning data and regression.

loop positioning uncertainty, it is likely that the device performance is better than we can measure with this setup.

4.3.5 Disturbance rejection

Disturbance rejection is another significant advantage from operating systems with feedback control. MEMS and other micro-scale devices are susceptible to normally insignificant environmental factors. Dust particles can impede motion, surface stiction can dominate other system forces, and delicate components can be easily fractured. The ability to automatically compensate for these complications will increase the reliability and robustness of many MEMS devices.

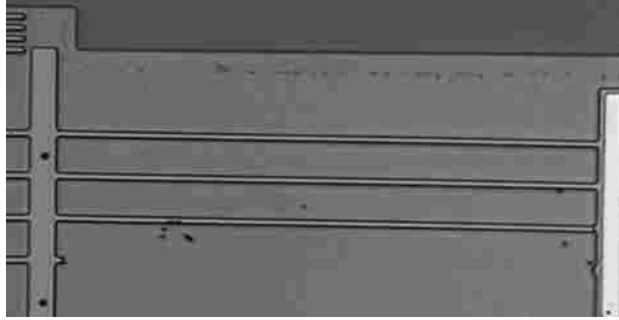

Figure 4.19: Optical micrograph of a TIM with one missing and one broken expansion beam to introduce a disturbance.

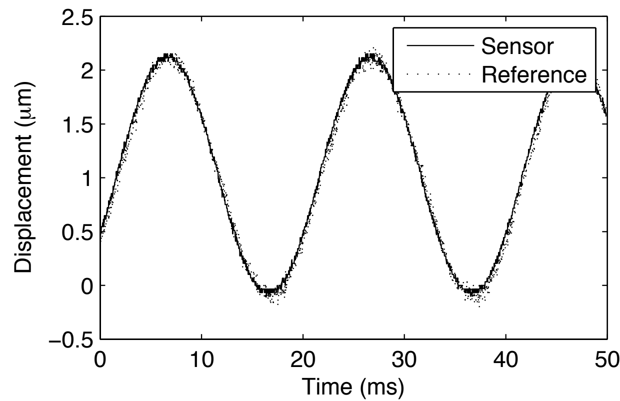

Figure 4.20: Closed-loop response of the broken TIM/PMT system shown in Figure 4.19. The system demonstrating insensitivity to the significant defects.

A TIM with one missing expansion leg and one broken expansion leg, as shown in Figure 4.19, was operated closed loop to demonstrate disturbance rejection. The same integral/lead controller, as described above, was used. Figure 4.20 is a plot of the input and output signals to the system. The excellent tracking, where the input and output signals are superimposed, demonstrates the system's insensitivity to the device defects.

4.4 Conclusion

It has been demonstrated that the PMT is an effective feedback sensor for closed-loop control of a MEMS thermal actuator. It has a monotonically increasing mapping of output voltage to displacement, and a repeatability of ±9.1 nm. The

PMT demonstrates that effective MEMS sensors can be constructed from uniformly doped polysilicon structures.

Feedback control of the TIM demonstrates the effectiveness of feedback control for MEMS devices, and particularly for thermal actuators. Feedback control reduced the rise time from 500 μs to 190 μs, provided excellent tracking with no steady-state error, maintained the positioning resolution to ± 29 nm or less, and increased the robustness of the system such that it was insensitive to significant damage.

Chapter 5

Conclusion

Integrated piezoresistive sensing enables the implementation of feedback control on MEMS devices. It provides all the benefits of improved performance, reliability, and robustness without the complications of large desk-top sensors, complex and unreliable on-chip sensors with poor signal-to-noise output, or expensive on-chip sensors fabricated from exotic materials. The Piezoresistive Flexure Model (PFM) facilitates the design of integrated piezoresistive sensing even into complex compliant structures.

This study has demonstrated how integrated piezoresistive sensors can be analyzed, designed into useful compliant MEMS devices, and used for feedback control to improve the performance of dynamically interesting systems.

5.1 Summary of Contributions

The research in this dissertation makes the following contributions related to integrated piezoresistive sensing of compliant MEMS devices.

- Validation of piezoresistive sensing's effectiveness for compliant MEMS devices via the measured piezoresistive response of a variety of MEMS devices.
- Development of an accessible predictive model, useful for design of long thin piezoresistive flexures.
- Validation of the piezoresistive model via the design and testing of a self-sensing long-displacement MEMS device.
- Identification of an effective feedback control scheme to improve the performance and reliability of the TIM.

- Implementation of feedback control, using integrated piezoresistive sensing, and verification of the predicted performance and reliability improvements.

5.2 Suggested Future Work

Integrated piezoresistive sensing has the potential to positively impact and enable many future MEMS technologies. We can increase our understanding of piezoresistive MEMS structures by examining their piezoresistive response to other types of loading conditions such as shear and torsion. It would also be useful to quantify the variability of PFM axial and bending piezoresistive coefficients. Investigating the applicability of the PFM to other piezoresistive materials, such as mono-crystalline silicon or even semiconducting carbon nanotubes, may lead to insights into why the bending response of polysilicon flexures is not as expected. In addition, a number of useful new MEMS devices can be designed utilizing integrated piezoresistive sensing using more sophisticated feedback control schemes.

Bibliography

[1] N. Maluf, *An Introduction to Microelectromechanical Systems Engineering.* Norwood, MA: Artech House, 2000. 1, 2, 3, 38, 39

[2] J. W. Gardner, V. K. Varadan, and O. O. Awadelkarim, *Microsensors MEMS and Smart Devices.* Wiley, 2001. 2

[3] S. E. Lyshevski, *Nano- and Microelectromechanical Systems.* CRC Press, 2001. 2

[4] M. J. Madou, *Fundamentals of Microfabrication, the Science of Miniaturization.* CRC Press, 2002. 2

[5] *SUMMiT V – Five Level Surface Micromachining Technology Design Manual*, 1st ed., MEMS Device and Reliability Physics Department, Microelectronics Development Laboratory, Sandia National Laboratories, PO Box 5800, Albuquerque, NM 87185, 22 September 2005. [Online]. Available: www.sandia.gov/mstc/education/alliance/tools/SUMMiT_V_Dmanual_V1.3_MASTER_external.pdf 2, 11, 39

[6] *PolyMUMPs Design Handbook*, MEMSCAP Inc., 2005. [Online]. Available: www.memsrus.com/documents/PolyMUMPs.DR.v11.pdf 2, 11, 28, 39, 40

[7] L. L. Howell, *Compliant Mechanisms.* New York, New York: Wiley, 2001. 2

[8] C. S. Smith, "Piezoresistance effect in germanium and silicon," *Physical Review*, vol. 94, pp. 42–49, 1954. 4, 9, 21, 38

[9] L. M. Roylance and J. B. Angell, "A batch-fabricated silicon accelerometer," *IEEE Transactions on Electron Devices*, vol. ED-26, no. 12, pp. 1911 – 1917, 1979. 4, 10

[10] W. P. Eaton, "Surface micromachined pressure sensors," Ph.D. dissertation, The University of New Mexico, Albuquerque, New Mexico, May 1997. 4, 10, 11, 38

[11] R. Schellin and G. Hess, "Silicon subminiature microphone based on piezoresistive polysilicon strain gauges," *Sensors and Actuators*, vol. 32, no. 1-3, pp. 555–559, 1992. 4, 10, 38

[12] D. Horsley, N. Wongkomet, R. Horowitz, and A. Pisano, "Precision positioning using a microfabricated electrostatic actuator," *IEEE Transactions on Magnetics*, vol. 35, pp. 993–999, 1999. 4, 37, 38

[13] S. Smith, D. Chetwynd, and S. Harb, "Simple two-axis ultraprecision actuator," *Review of Scientific Instruments*, vol. 65, no. 4 pt 1, pp. 910 – 917, 1994. [Online]. Available: http://dx.doi.org/10.1063/1.1144920 4

[14] R. K. Messenger, T. W. McLain, and L. L. Howell, "Feedback control of a thermomechanical inplane microactuator using piezoresistive displacement sensing," *American Society of Mechanical Engineers, Dynamic Systems and Control Division (Publication) DSC*, vol. 73, no. 2 PART B, pp. 1301 – 1310, 2004. 5, 40

[15] ——, "Improved nanopositioning resolution through piezoresistive feedback control of a MEMS thermal actuator," *American Society of Mechanical Engineers, Dynamic Systems and Control Division (Publication) DSC*, vol. 74 DSC, no. 2 PART B, pp. 1327 – 1334, 2005. 5, 6, 40, 45, 53, 55

[16] ——, "Piezoresistive feedback for improving transient response of mems thermal actuators," *Proceedings of SPIE - The International Society for Optical Engineering*, vol. 6174 I, pp. 617 408 –, 2006. [Online]. Available: http://dx.doi.org/10.1117/12.657954 5, 6, 47

[17] M. M. Mandurah, K. C. Saraswat, and T. I. Kamins, "Model of conduction in polycrystalline silicon - 1: Theory." *IEEE Transactions on Electron Devices*, vol. ED-28, no. 10, pp. 1163 – 1171, 1981. 10

[18] ——, "Model for conduction in polycrystalline silicon - 2: Comparison of theory and experiment." *IEEE Transactions on Electron Devices*, vol. ED-28, no. 10, pp. 1171 – 1176, 1981. 10

[19] V. Gridchin and V. Lubimskij, "Phenomenological model of the piezoresistive effect in polysilicon films," *Mikroelektronika*, vol. 32, no. 4, pp. 261 – 271, 2003. [Online]. Available: http://dx.doi.org/10.1023/A:1024567213980 10, 12, 38

[20] P. Kleimann, B. Semmache, M. Le Berre, and D. Barbier, "Stress-dependent hole effective masses and piezoresistive properties of p-type monocrystalline and polycrystalline silicon," *Physical Review B: Condensed Matter*, vol. 57, no. 15, pp. 8966 –, 1998. [Online]. Available: http://dx.doi.org/10.1103/PhysRevB.57.8966 10

[21] T. L. Waterfall, "Design of piezoresistive MEMS force and displacement sensors," Master's thesis, Brigham Young University, Provo, UT, 2006. [Online]. Available: http://contentdm.lib.byu.edu/ETD/image/etd1549.pdf 10, 11, 13, 15, 16, 19

[22] L. Ristic, R. Gutteridge, B. Dunn, D. Mietus, and P. Bennett, "Surface micromachined polysilicon accelerometer," pp. 118 – 121, 1992, polysilicon accelerometers;Polysilicon layers;. [Online]. Available: http://dx.doi.org/10.1109/SOLSEN.1992.228311 11, 38

[23] K. Kwon and S. Park, "Three axis piezoresistive accelerometer using polysilicon layer," *International Conference on Solid-State Sensors and Actuators, Proceedings*, vol. 2, pp. 1221 – 1224, 1997. 11, 38

[24] H. Guckel, "Surface micromachined pressure transducers," *Sensors and Actuators A*, vol. 28, pp. 133–146, 1991. 11, 38

[25] J. W. Wittwer, T. Gomm, and L. L. Howell, "Surface micromachined force gauges: Uncertainty and reliability," *Journal of Micromechanics and Microengineering*, vol. 12, no. 1, pp. 13 – 20, 2002, surface micromachined force gauges;Uncertainty;Probabilistic design;Force gauge model;Force uncertainty;. [Online]. Available: http://dx.doi.org/10.1088/0960-1317/12/1/303 14, 23

[26] G. K. Johns, "The piezoresistive effect in microflexures," Master's thesis, Brigham Young University, Provo, UT, April 2007. [Online]. Available: http://contentdm.lib.byu.edu/ETD/image/etd1673.pdf 16

[27] T. Shoup and C. McLarnan, "On the use of the undulating elastica for the analysis of flexible link mechanisms," *Journal of Engineering for Industry*, pp. 263 – 7, 1971. 20

[28] N. B. Hubbard, J. W. Wittwer, J. A. Kennedy, D. L. Wilcox, and L. L. Howell, "A novel fully compliant planar linear-motion mechanism 57008," *Proceedings of the ASME Design Engineering Technical Conference*, vol. 2 A, pp. 1 – 5, 2004. 25

[29] G. Subhash, A. D. Corwin, and M. P. Deboer, "Operational wear and friction in mems devices," *American Society of Mechanical Engineers, Micro-Electro Mechanical Systems Division, (Publications) MEMS*, pp. 207 – 209, 2004. 26

[30] D. Senft, M. Dugger, and B. Smith, "Friction and wear in lubricated mems," *American Society of Mechanical Engineers, Materials Division (Publication) MD*, vol. 84, pp. 123 – 125, 1998, friction coefficients;. 26

[31] J. R. Cannon, C. P. Lusk, and L. L. Howell, "Compliant rolling-contact element mechanisms," *Proceedings of the ASME International Design Engineering Technical Conferences and Computers and Information in Engineering Conference - DETC2005*, vol. 7 A, pp. 3 – 13, 2005. 26, 28

[32] M. J. Daneman, N. C. Tien, O. Solgaard, A. P. Pisano, K. Y. Lau, and R. S. Muller, "Linear microvibromotor for positioning optical components," *Journal of Microelectromechanical Systems*, vol. 5, no. 3, pp. 159 – 165, 1996. [Online]. Available: http://dx.doi.org/10.1109/84.536622 28, 37

[33] M. Baltzer, T. Kraus, and E. Obermeier, "Linear stepping actuator in surface micromachining technology for low voltages and large displacements," vol. 2, Chicago, IL, USA, 1997, pp. 781 – 784. [Online]. Available: http://dx.doi.org/10.1109/SENSOR.1997.635216 28

[34] R. Yeh, S. Hollar, and K. S. Pister, "Single mask, large force, and large displacement electrostatic linear inchworm motors," *Journal of Microelectromechanical Systems*, vol. 11, no. 4, pp. 330 – 336, 2002. [Online]. Available: http://dx.doi.org/10.1109/JMEMS.2002.800937 28

[35] J. M. Maloney, D. S. Schreiber, and D. L. DeVoe, "Large-force electrothermal linear micromotors," *Jornal of Micromechanics and Microengineering*, vol. 14, pp. 226–234, November 2003. 28, 39

[36] T. L. Waterfall, G. K. Johns, R. K. Messenger, B. D. Jensen, T. W. McLain, and L. L. Howell, "Observations of piezoresistivity for polysilicon in bending that are unexplained by current models," *Sensors and Actuators, A: Physical*, 2007, in Review. 32

[37] G. K. Johns, L. L. Howell, B. D. Jensen, and T. W. McLain, "A model for predicting the piezoresistive effect in microflexures experiencing bending and tension loads," *Journal of Microelectromechanical Systems*, 2007, in Press. 32

[38] B. Borovic, A. Liu, D. Popa, H. Cai, and F. Lewis, "Open-loop versus closed-loop control of mems devices: Choices and issues," *Journal of Micromechanics and Microengineering*, vol. 15, no. 10, pp. 1917 – 1924, 2005, feedback design;Sensor data;Actuator dynamics;System dynamics;. [Online]. Available: http://dx.doi.org/10.1088/0960-1317/15/10/018 37

[39] T. Hirano, L. Fan, W. Lee, J. Hong, W. Imaino, S. Pattanaik, S. Chan, P. Webb, R. Horowitz, S. Aggarwal, and D. Horsley, "High-bandwidth high-accuracy rotary microactuators for magnetic hard disk drive tracking servos," *IEEE/ASME Transactions on Mechatronics*, vol. 3, no. 3, pp. 156–165, 1998. 37

[40] D. Horsley, R. Horowitz, and A. Pisano, "Microfabricated electrostatic actuators for hard disk drives," *Proceedings of the IEEE Conference on Decision and Control*, vol. 4, pp. 3120–3125, 2000. 37

[41] Y. Li and R. Horowitz, "Track-following controller design of MEMS based dual-stage servos in magnetic hard disk drives," *Proceedings - IEEE Conference on Robotics and Automation*, vol. 1, pp. 953–958, 2000. 37

[42] T. Semba, T. Hirano, J. Hong, and L. Fan, "Dual-stage servo controller for HDD using MEMS microactuator," *IEEE Transactions on Magnetics*, vol. 35, no. 5, pt. 1, pp. 2271–2273, 1999. 37

[43] Y. Sun, K. Piyabongkam, A. Sezen, B. Nelson, R. Rajamani, R. Schoch, and D. Potasek, "A novel dual-axis electrostatic microactuation system for micromanipulation," *IEEE International Conference on Intelligent Robots and Systems*, vol. 2, pp. 1796–1801, 2002. 37, 38

[44] S. Lyshevski, "Nonlinear Microelectromechanical Systems (MEMS) analysis and design via the Lyapunov stability theory," *Proceedings of the IEEE Conference on Decision and Control*, vol. 5, pp. 4681–4684, 2001. 37

[45] M. S.-C. Lu and G. K. Fedder, "Position control of parallel-plate microactuators for probe-based data storage," *Journal of Microelectromechanical Systems*, vol. 13, no. 5, pp. 759 – 769, 2004, cMOS-MEMS;Electrostatic pull in;Capacitive sensor;Nonlinear plant;Unstable pole;. [Online]. Available: http://dx.doi.org/10.1109/JMEMS.2004.835761 37

[46] S. Bhansali, A. L. Zhang, R. B. Zmood, P. E. Jones, and D. K. Sood, "Prototype feedback-controlled bidirectional actuation system for mems applications," *Journal of Microelectromechanical Systems*, vol. 9, no. 2, pp. 245 – 251, 2000, prototype feedback controlled bidirectional actuation system;Beam mass structure;Inductive sensor;Magnetic actuator;Magnetic microsuspension system;Micromagnetic bearing;Position sensor;. [Online]. Available: http://dx.doi.org/10.1109/84.846705 37

[47] M. Pai and N. C. Tien, "Operating principles of an electrothermal vibromotor for optical switching applications," *Proceedings of SPIE - The International Society for Optical Engineering*, vol. 3878, pp. 124 – 130, 1999, electrothermal vibromotor;Polysilicon surface micromachined;Low voltage square wave signal;Thermal actuation;Micromirror;. [Online]. Available: http://dx.doi.org/10.1117/12.361253 37

[48] J. C. Chiou and W. T. Lin, "Variable optical attenuator using a thermal actuator array with dual shutters," *Optics Communications*, vol. 237, no. 4-6, pp. 341–350, July 2004. 37, 40

[49] B.-H. Kim and K. Chun, "Fabrication of an electrostatic track-following micro actuator for hard disk drives using soi wafer," *Journal of Micromechanics and Microengineering*, vol. 11, no. 1, pp. 1 – 6, 2001. [Online]. Available: http://dx.doi.org/10.1088/0960-1317/11/1/301 37

[50] P. Cheung, R. Horowitz, and R. Howe, "Design, fabrication, position sensing, and control of an electrostatically-driven polysilicon microactuator," *IEEE Transactions on Magnetics*, vol. 32, pp. 122–128, 1996. 38

[51] L. Cao, T. S. Kim, J. Zhou, S. C. Mantell, and D. L. Polla, "Calibration technique for MEMS membrane type strain sensors," *Biennial University/Government/Industry Microelectronics Symposium - Proceedings*, pp. 204 – 210, 1999. [Online]. Available: http://dx.doi.org/10.1109/UGIM.1999.782854 38

[52] H. Joseph, B. Swafford, and S. Terry, "MEMS in the medical world," *Sensors*, vol. 14, no. 4, pp. 47–51, 1997. 38

[53] R. Cragun, "Constrained thermal expansion micro-actuator," *ASME, Dynamic Systems and Control Division (DSC), 66, Micro-Electro-Mechanical Systems (MEMS)*, no. 365 - 371, 1998. 39, 40

[54] L. Que, A. Otradovec, and Y. Gianchandani, "Pulse and DC operation lifetimes of bent-beam electrothermal actuators," *Proceedings of the IEEE Micro Electro Mechanical Systems (MEMS)*, pp. 570–573, 2001. 39

[55] L. Que, J. Park, and Y. Gianchandani, "Bent-beam electrothermal actuators - part I: Single beam and cascaded devices," *Journal of Microelectromechanical Systems*, vol. 10, no. 2, pp. 247–254, 2001. 39

[56] C. Lott, T. W. McLain, J. N. Harb, and L. L. Howell, "Modeling the thermal behavior of a surface-micromachined linear-displacement thermomechanical microactuator," *Sensors and Actuators*, vol. 101, no. 1-2, pp. 239–250, 2002. 39, 40, 41, 49, 50, 55

[57] A. A. Geisberger, N. Sarkar, M. Ellis, and G. D. Skidmore, "Electrothermal properties and modeling of polysilicon microthermal actuators," *Journal of Microelectromechanical Systems*, vol. 12, no. 4, pp. 513–523, August 2003. 39, 40, 41, 47, 49, 50

[58] R. Hickey, D. Sameoto, T. Hubbard, and M. Kujath, "Time and frequency response of two-arm micromachined thermal actuators," *Journal of Micromechanics and Microengineering*, vol. 13, pp. 40–46, 2002. 39, 40

[59] J. H. Comtois, V. M. Bright, and M. W. Phipps, "Thermal microactuators for surface-micromachining processes," *Proceedings of SPIE - The International Society for Optical Engineering*, vol. 2642, pp. 10 – 21, 1995. 39

[60] R. Legtenberg, A. Groeneveld, and M. Elwenspoek, "Comb-drive actuators for large displacements," *Journal of Micromechanics and Microengineering*, vol. 6, no. 3, pp. 320–329, 1996. 39

[61] M. S. Baker and L. L. Howell, "On-chip actuation of an in-plane compliant bistable micro-mechanism," *Journal of Microelectromechanical Systems*, vol. 11, no. 5, pp. 566–573, 2002. 39, 40

[62] B. D. Jensen and L. L. Howell, "Identification of compliant pseudo-rigid-body mechanism configurations resulting in bistable behavior," *Jornal of Mechanical Design*, vol. in press, 2003. 40

[63] N. D. Masters and L. L. Howell, "A self-retracting fully-compliant bistable micromechanism," *Journal of Microelectromechanical Systems*, vol. 12, no. 3, pp. 273–280, 2003. 40

[64] C. Lee, Y.-S. Lin, Y.-J. Lai, M. H. Tasi, C. Chen, and C.-Y. Wu, "3-V driven pop-up micromirror for reflecting light toword out-of-plane direction for VOA applications," *IEEE Photonics Technology Letters*, vol. 16, no. 4, April 2004. 40

[65] L. Que, K. Udeshi, J. Park, and Y. B. Gianchandani, "A bistable electro-thermal RF switch for high power applications," *Proceedings of the IEEE Micro Electro Mechanical Systems (MEMS)*, pp. 797–800, 2004. 40

[66] Y. Wang, Z. Li, D. T. McCormick, and N. C. Tien, "A low-voltage lateral MEMS switch with high RF performance," *Journal of Microelectromechanical Systems*, vol. 13, no. 6, December 2004. 40

[67] N. B. Hubbard and L. L. Howell, "Experimental repeatability of a thermal actuator for nanopositioning," *American Society of Mechanical Engineers, Micro-Electro Mechanical Systems Division, (Publications) MEMS*, pp. 427 – 430, 2004. 40, 46

[68] R. K. Messenger, "Modeling and control of surface micromachined thermal actuators," Master's thesis, Brigham Young University, August 2004. [Online]. Available: http://contentdm.lib.byu.edu/ETD/image/etd434.pdf 40, 41, 47, 49, 50

[69] L. Lin and M. Chiao, "Electrothermal responses of lineshape microstructures," *Sensors and Actuators*, vol. 55, pp. 35–41, 1996. 41

[70] J. W. Wittwer, M. S. Baker, and L. L. Howell, "Simulation, measurement, and asymmetric buckling of thermal microactuators," *Sensors and Actuators, A: Physical*, vol. 128, no. 2, pp. 395 – 401, 2006. [Online]. Available: http://dx.doi.org/10.1016/j.sna.2006.02.014 43

[71] G. F. Franklin, J. D. Powell, and A. Emami-Naeini, *Feedback control of dynamic systems*, 3rd ed. Addison Wesley, 1995. 54